Aalborg Universitet

AALBORG UNIVERSITY
DENMARK

Small Signal Modeling and Comprehensive Analysis of Magnetically Coupled Impedance Source Converters

Forouzesh, Mojtaba; Siwakoti, Yam Prasad; Blaabjerg, Frede; Hasanpour, Sara

Small-Signal Modeling and Comprehensive Analysis of Magnetically Coupled Impedance-Source Converters

Mojtaba Forouzesh, *Student Member, IEEE*, Yam P. Siwakoti, *Member, IEEE*,
Frede Blaabjerg, *Fellow, IEEE*, and Sara Hasanpour

Abstract—**Magnetically coupled impedance-source (MCIS) networks are recently introduced impedance networks intended for various high-boost applications. It employs coupled magnetic in the circuit to achieve higher voltage gain. Various MCIS networks have been proposed in the literature for myriad applications; however, due to effective role of system modeling in the closed-loop controller design, this paper is allocated to small-signal modeling and analysis of MCIS converters. The modeling is performed by means of the circuit averaging and averaged switch technique. A generalized small-signal derivation is demonstrated for pulse width modulation (PWM) MCIS converters and it is shown that the derived transfer functions can simply be applied to Y-source, Γ-source, and T-source impedance networks. Various transfer functions for capacitor voltage, output voltage, magnetizing current, input and output impedance are derived and have been validated through frequency and dynamic responses of computer simulation results. In addition, a comprehensive analysis has been done for all mentioned PWM MCIS converters regarding their circuit parameters. Furthermore, the effect of considering the equivalent series resistances of capacitor and inductor on the stability margin of MCIS converters is revealed in this paper. Finally, in order to validate the derived transfer functions and to consolidate the perfumed analysis, experimental results are presented for all mentioned MCIS converters.**

Index Terms—**Circuit averaging technique, dynamic response, frequency response, magnetically coupled impedance-source (MCIS) network, nonminimum phase (NMP) zero, small-signal modeling.**

I. INTRODUCTION

MAGNETICALLY coupled impedance-sources (MCIS) are newborn impedance networks that can provide unique features such as their forerunner, Z-source converter. Simultaneous buck/boost ability, high immunity to disturbances, and simple seamless control are some primary characteristics for MCIS converters. However, due to the utilization of coupled

inductors, the main merits of MCIS converters are their high-voltage boost ability, circuit integrity, and small size/weight [1]. Some major MCIS networks namely Γ-source, T-source, and Y-source have distinct voltage boost characteristics. The voltage gain of Γ-source increases by decrease in the turns ratio [2], on the other hand, the voltage gain of T-source increases by increasing of the turns ratio [3], different from both, the voltage gain of Y-source increases by both increasing and decreasing of its turns ratios [4]. Up to now, steady state and dc characteristics of MCIS converters have been investigated in many articles [5], [6]. However, there is no detailed modeling and analysis of MCIS converters.

Because of demands for closed-loop control design and stability assessment of the power converters, the necessity of small-signal modeling is evident to engineers and control designers. Various small-signal modeling methods have been introduced in the literature, namely state-space averaging [7], switch pulse width modulation (PWM) technique [8], signal flow graph [9], and energy factor [10]. Among them, the switch PWM approach is a viable solution to derive small-signal model of a PWM circuit containing small number of semiconductor switches and diodes, as it gives a better insight of the circuit behavior [11], [12]. The advantage of switch PWM modeling approach on MCIS converters reveals where the same model can be used for various converters, and there is no need to rederive the obtained transfer functions for other MCIS converters. Another merit of this approach is that the equivalent series resistance (ESR) of reactive components can simply be included in the derived transfer functions so that the effects of ESRs on the output frequency response can be evaluated too.

As can be found in the literature, small-signal modeling and control aspects of the Z-source family have been investigated thoroughly by various approaches [13]. In [14], signal flow graph approach was used to drive transfer function of the switched Z-source impedance network. In [15] and [16], state-space averaging method was used to derive small-signal model of Z-source converter. In [17], small-signal modeling of PWM Z-source converter is obtained by the circuit averaging technique. However, only few papers are found in the literature to address this small-signal modeling of MCIS converters. In [18] and [19], small-signal modeling of trans-Z-source and improved trans-Z-source inverters has been presented by means of a state-space averaging method, respectively. However, a comprehensive modeling, analysis, and comparison of dynamic and stability behavior of MCIS converters are still missed in the

Fig. 1. Generic structure of MCIS converters.

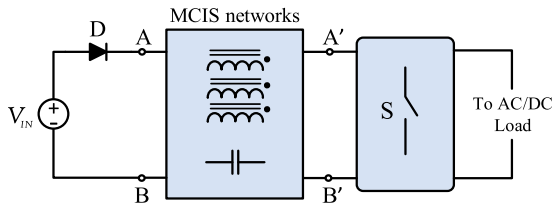Fig. 2. PWM Y-source converter with perturbation in the input voltage, duty cycle, and the load current.

literature. Considering the significance of control aspects of the impedance-source-based converters [13], this paper is devoted to comprehensive derivation of ac small-signal modeling and analysis of MCIS-based converters. Fig. 1 illustrates a generic configuration of MCIS converters, in which the switch S consist of either a single switch or single/three-phase inverter bridge for dc or ac output.

The modeling of MCIS inverters can be divided into two sides, dc-side and ac-side. To reduce system complexity, the dynamic analysis of the dc and ac sides can be investigated separately. Since the small-signal modeling of ac-side of impedance-source inverters has been investigated before [20], [21], this paper focuses only on the modeling of the dc-side of MCIS inverters which is more challenging to control designers that have not been thoroughly investigated. The dc-side of impedance-source-based inverters can be controlled through direct [22] or indirect single loop, dual loop, and multiloop control strategies [23]–[25]. From the literature, it can be inferred that indirect control methods are more interesting due to their promising performance in control of impedance-source-based converters. Each control method has its merits and demerits, which demand different implantation strategies. To this end, various transfer functions needed to be extracted for different control strategies.

The major contributions of this paper are summarized as: 1) derivation and validation of a generalized average large signal, dc and ac small-signal linear model for MCIS converters; 2) derivation and validation of various transfer functions of MCIS converters; 3) comparative study and analysis of the dynamic and stability behavior of the mentioned MCIS converters. This helps readers to understand the insights of various MCIS networks better for control and system design.

In the following sections, a detailed small-signal model for Y-source converter operating in continuous conduction mode (CCM) is presented by means of the averaged switch PWM modeling approach. It is shown that the derived small-signal model and transfer functions related to the PWM Y-source converter can simply be developed to other MCIS converters. In Section II, a generalized derivation of the small-signal model of PWM MCIS converters operating in CCM is presented. The derivation of open-loop input voltage to capacitor voltage, output voltage, and magnetizing current transfer functions; control to capacitor voltage, output voltage, and magnetizing current transfer functions; input and output impedances are presented in Section III. Section IV provides some computer verification of the average model and the derived transfer functions for all studied MCIS converters. A comprehensive analysis and comparison of the frequency response and stability margin of various PWM MCIS converters are presented in Section V. Experimental validation for all studied MCIS converters is provided in Section VI and finally this paper is concluded in Section VII.
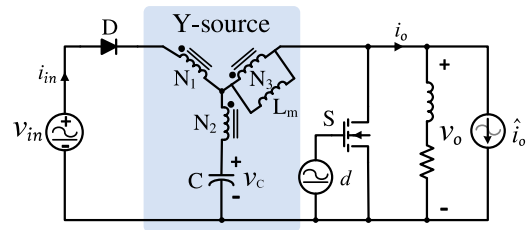
II. DERIVATION OF THE SMALL-SIGNAL MODEL FOR THE PWM MCIS CONVERTERS

In Fig. 1, by replacing switch S with a single MOSFET and modeling the load with a current source, the MCIS converters turn into PWM converters that can be modeled by the averaged switch PWM circuit modeling approach. Fig. 2 shows PWM Y-source converter considering ac perturbation for input voltage ($\hat{v}_{in}$), duty cycle ($\hat{d}$), and load current ($\hat{i}_o$). In Fig. 2, the symbol $\sim$ stands for average value (dc part) plus perturbation (ac part). There are some predominant notations in the following of this paper, namely $v_{in} = V_{IN} + \hat{v}_{in}$, $i_{in} = I_{IN} + \hat{i}_{in}$, $v_o = V_O + \hat{v}_o$, $i_o = I_O + \hat{i}_o$, and $d = D + \hat{d}$. In which, capital quantities are averaged values and quantities with "hat" are perturbation values. Apparently, quantities with "hat" are time-variant values, when are added to its average values, lead to an overall time-variant quantity. In order to simplify notations, subscript "(t)" is neglected for all time-variant quantities.

It is to be noted that all small-signal derivation for Γ-source and T-source can be derived later from the Y-source small-signal model. Hence, in the following of this section, the derivation is only conducted for the PWM Y-source converter. As shown in Fig. 3, by letting the respective winding equal to zero, all setup and derivations will transformed to the related MCIS.

Following assumptions are dominant in the small-signal modeling and transfer function derivations:
1) PWM MCIS converters are operating in CCM;
2) all passive components are lossless and coupling coefficients of the coupled inductors are perfect. (This is quite reasonable since MCISs normally demand tightly coupled magnetics, besides, when transfer functions are derived in impedance form, the ESRs can be added to the transfer functions);
3) all semiconductor switches, diodes, and MOSFETs are ideal and V_D and R_{on} are negligible;
4) the natural time constant of the MCIS converters is much longer than one switching period.

The main nonlinear components in the PWM Y-source converter are diode D and MOSFET S; other components like capacitor, coupled inductors, and resistor are linear and time invariant. The first step in a switch PWM modeling approach is to pull out the switching components from the other circuit elements. Then, an average circuit model can be find in order to linearize the switch network. Fig. 4 shows the PWM Y-source converter with
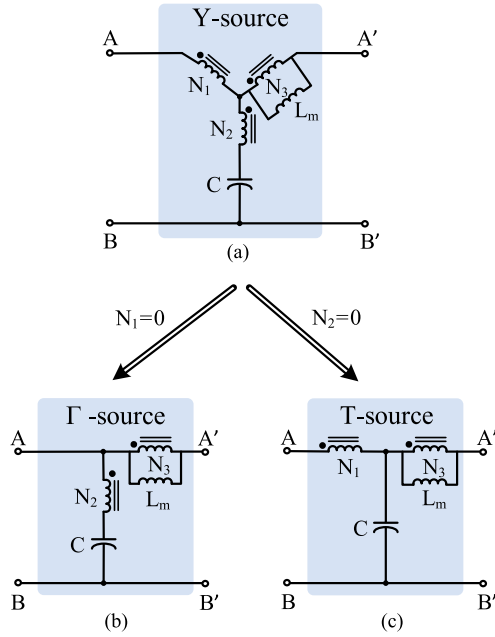
Fig. 3. Derivation of two winding MCIS networks: (b) Gamma Source and (c) T-source from a (a) Y-source network.
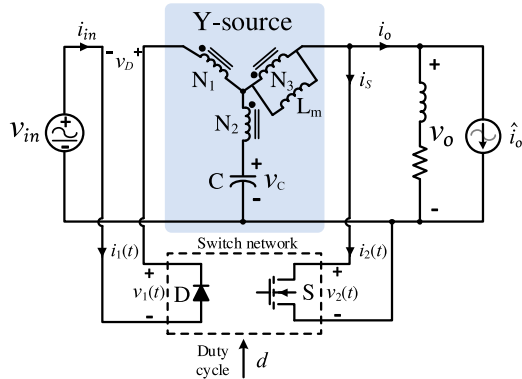

Fig. 4. PWM Y-source converter with illustration of the nonlinear switch network.

TABLE I
VARIOUS WINDING CONFIGURATIONS OF Y-SOURCE NETWORK

$K = \frac{N_3+N_1}{N_3-N_2}$	$0 < D < D_{\max}$	$V_o\,(peak)/V_{\text{IN}}$	$N_1 : N_2 : N_3$
3	$0 < D < 1/3$	$(1-3D)^{-1}$	1:1:2, 3:1:3, 1:3:5
4	$0 < D < 1/4$	$(1-4D)^{-1}$	2:1:2, 1:2:3, 5,1:3
5	$0 < D < 1/5$	$(1-5D)^{-1}$	3:1:2, 2:2:3, 1:3:4
6	$0 < D < 1/6$	$(1-6D)^{-1}$	3:2:3, 2:3:4, 4:1:2
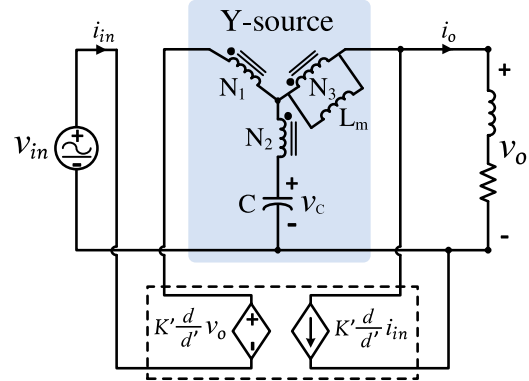
Fig. 5. Averaged large-signal model of the PWM Y-source converter.

the dc-link voltage of in its inverter. The average value of the output voltage (V_O) is equal to the average value of the capacitor voltage (V_C). Hence, according to the steady-state analysis of the Y-source network, assuming the voltage across L_3 is V_L, the voltage of capacitor C can be obtained by applying volt–second balance principle to the inductor voltage V_L. Besides, the magnetizing current on the third winding can be obtained from the capacitor C charge balance principle [26]

$$V_C = V_O = \frac{1-D}{1-KD} V_{\text{IN}} \qquad (1)$$

$$I_M = \frac{N_1 + N_3}{N_3} I_{\text{IN}}. \qquad (2)$$

In (1), D is the duty cycle of shoot-through mode and K is the winding factor of Y-source impedance network which can be defined as $K = (N_3 + N_1)/(N_3 - N_2)$. Apparently, the voltage gain of the Y-source converter can be varied by various winding factor. Some features of Y-source impedance network with various winding configurations of the coupled inductors for different winding factors are noted in Table I. For a lossless circuit $(V_{\text{IN}} I_{\text{IN}} = V_O I_O)$, according to (1), the averaged output current of the PWM Y-source converter can be obtained

$$I_O = \frac{1-KD}{1-D} I_{\text{IN}}. \qquad (3)$$

Considering (1) and (3), by using Kirchhoff's voltage and current laws in both shoot-through and nonshoot-through modes, the averaged values of the voltage across diode D and the current that pass through MOSFET S are obtained

$$V_D = K' \frac{D}{D'} V_O \qquad (4)$$

$$I_S = K' \frac{D}{D'} I_{\text{IN}}. \qquad (5)$$

extracted two port switch network from the circuit. As shown in Fig. 4, terminal quantities at the two side of the switch network are $v_1(t)$, $i_1(t)$, $v_2(t)$ and $i_2(t)$. At each side, one quantity can be selected as an independent input, and, hence, the two other quantities would be dependent inputs. However, the selection of independent quantities is arbitrary; it is typically common to select the current of diode and the voltage of MOSFET as independent quantities. Besides, the duty cycle d would be as the independent control input. As can be found from Fig. 3, four terminal voltages and currents of the PWM Y-source converter are as $v_1(t) = v_D$, $i_1(t) = i_{\text{in}}$, $v_2(t) = v_o$, and $i_2(t) = i_S$. As defined before, $i_1(t)$ and $v_2(t)$ are independent quantities, the next step is to find dependent quantities $v_1(t)$ and $i_2(t)$ as functions of independents quantities [11]. Consequently, v_D and i_S are dependent values of the switch network that should be written solely based on dependent values v_O and i_{in}.

Due to the existence of shoot-through modes in impedance source based converters, the output voltage of PWM Y-source converter is pulsating, which its peak value is equivalent to

Fig. 6.   Dc and ac small-signal model of open-loop PWM Y-source converter operating in CCM.

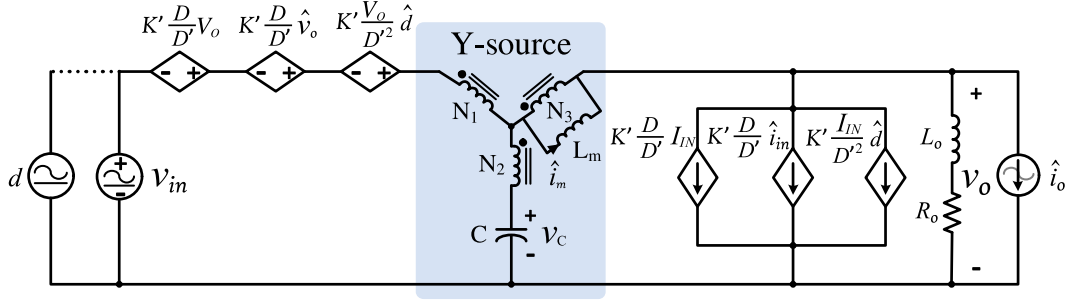In (4) and (5), D' is the duty cycle of nonshoot-through mode and defined as $D' = 1 - D$. As well as K' is the winding coefficient of the Y-source which is introduced to simplify the following derivations and can be defined as $K' = (N_1 + N_2)/(N_3 - N_2)$. Equations (4) and (5) represent the dc model for switch network. By substituting with time-variant values and using approximation, the ac large-signal model of the switch network can be written as follows:

$$v_D \approx K' \frac{d}{d'} v_o \qquad (6)$$

$$i_S \approx K' \frac{d}{d'} i_{\text{in}}. \qquad (7)$$

In (6) and (7), v_D and i_S are large signal time-variant quantities that defined as $v_D = V_D + \hat{v}_D$ and $i_S = I_S + \hat{i}_S$. Fig. 5 illustrates the averaged large-signal model of the PWM Y-source converter.

Considering small-signal ac components for all quantities in (6) and (7), we have

$$v_D = V_D + \hat{v}_D = K' \frac{D + \hat{d}}{D' - \hat{d}} (V_O + \hat{v}_o) \qquad (8)$$

$$i_S = I_S + \hat{i}_S = K' \frac{D + \hat{d}}{D' - \hat{d}} \left(I_{\text{IN}} + \hat{i}_{\text{in}} \right). \qquad (9)$$

Expanding the second term in (8) and (9), and using the first-order approximation for McLaurin series, the following equation is achieved:

$$\frac{D + \hat{d}}{D' - \hat{d}} = \frac{D + \hat{d}}{D'} \frac{1}{1 - \frac{\hat{d}}{D'}} = \frac{D + \hat{d}}{D'} \left(1 + \frac{\hat{d}}{D'} \right). \qquad (10)$$

Substituting (10) into (8) and (9), we have

$$v_D = K' \frac{D + \hat{d}}{D'} \left(1 + \frac{\hat{d}}{D'} \right) (V_O + \hat{v}_o) \qquad (11)$$

$$i_S = K' \frac{D + \hat{d}}{D'} \left(1 + \frac{\hat{d}}{D'} \right) \left(I_{\text{IN}} + \hat{i}_{\text{in}} \right). \qquad (12)$$

Expanding (11) and (12), and neglecting the terms with multiplied of two perturbation signals, lead to both dc and ac small-signal model of the switch network of PWM Y-source converter
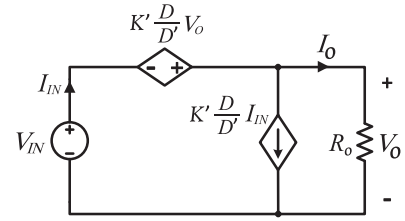
Fig. 7.   Dc model of open-loop PWM Y-source converter operating in CCM.
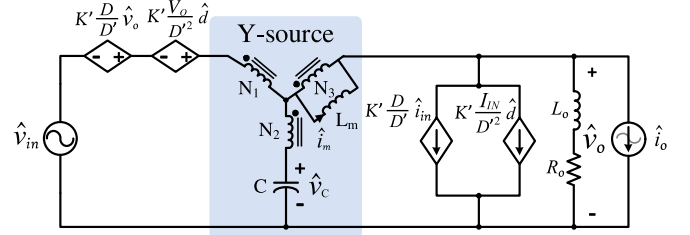
Fig. 8.   Ac small-signal model of open-loop PWM Y-source converter operating in CCM.

operating in CCM

$$v_D = K' \frac{D}{D'} V_O + K' \frac{D}{D'} \hat{v}_o + K' \frac{V_O}{D'^2} \hat{d} \qquad (13)$$

$$i_S = K' \frac{D}{D'} I_{\text{in}} + K' \frac{D}{D'} \hat{i}_{\text{in}} + K' \frac{I_{\text{IN}}}{D'^2} \hat{d}. \qquad (14)$$

The first term in (13) and (14) represent the dc model and the second and third terms in (13) and (14) represent ac small-signal linear model of diode D and MOSFET S. Linearization is realized by omitting second-order terms of ac perturbed signals in (11) and (12). Now, the dc and ac small-signal model of the PWM Y-source converter can be realized using voltage and current controlled sources. Fig. 6 illustrated the dc and linear small-signal model of the PWM Y-source converter operating in CCM. Furthermore, the dc model and ac model of the PWM Y-source converter are illustrated in Figs. 7 and 8, respectively.

III. SMALL-SIGNAL EQUIVALENT CIRCUITS AND DERIVATION OF TRANSFER FUNCTIONS

A. Input Voltage to Capacitor Voltage Transfer Function

In order to derive the transfer functions from input voltage perturbation, $\hat{d}$ must be ignored in the ac small-signal model

Fig. 9. Ac small-signal model to derive input voltage to capacitor voltage/magnetizing current transfer functions.

of PWM Y-source converter. In addition, for the following derivation in this section, it is assumed that there is no perturbation in load current. Hence, letting $\hat{d} = 0$ and $\hat{i}_o = 0$ in Fig. 8, the ac small-signal model to derive input voltage to capacitor voltage, output voltage, and magnetizing current transfer functions can be achieved as shown in Fig. 9. The impedance of coupled inductors is considered as a single impedance (Z_m) on the third winding 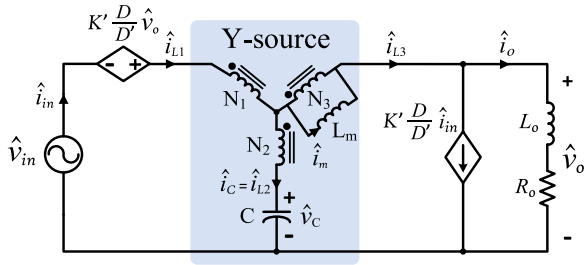of all PWM MCIS converters. The impedances of the ideal magnetizing inductor (L_m) and the ideal capacitor C are expressed as

$$Z_m = sL_m \tag{15}$$

$$Z_C = \frac{1}{sC}. \tag{16}$$

Moreover, in order to perform a practical analysis, after the transfer functions are derived in their impedance form, the ESRs of magnetizing inductor (ESR_L) and capacitor C (ESR_C) can be added to their impedances. The load impedance is considered as (17). It should be noted that the perturbation in load current can be implemented through the load impedance (Z_o)

$$Z_o = R_o + sL_o. \tag{17}$$

As it is known, in a three winding coupled inductor, the following equation is dominant:

$$N_1 i_{L1} + N_2 i_{L2} + N_3 i_{L3} = 0. \tag{18}$$

From Fig. 9, applying Kirchhoff's current law (KCL) and using (18), the following equations can be written:

$$\hat{i}_{\text{in}} = \frac{\hat{i}_C + \hat{i}_o}{1 - K'\frac{D}{D'}} \tag{19}$$

$$\hat{i}_m = \frac{N_2}{N_3}\hat{i}_C + \left(\frac{N_1}{N_3} + K'\frac{D}{D'}\right)\hat{i}_{\text{in}} + \hat{i}_o. \tag{20}$$

Applying Kirchhoff's voltage law (KVL) on the right and left loops of the circuit in Fig. 9, the following equations can be written:

$$\hat{v}_o + \left(\frac{N_3 - N_2}{N_3}\right)\hat{v}_m - \hat{v}_C = 0 \tag{21}$$

$$\hat{v}_C + \left(\frac{N_1 + N_2}{N_3}\right)\hat{v}_m - \hat{v}_{\text{in}} - K'\frac{D}{D'}\hat{v}_o = 0. \tag{22}$$

Considering Ohm's law for the voltage across magnetizing inductor, capacitor C and output voltage, and using (19) to (22), the input voltage to capacitor voltage transfer function (G_{Vcv}) is derived in the impedance form as given by

$$G_{\text{Vcv}} = \frac{\hat{v}_C}{\hat{v}_{\text{in}}}$$

$$= \frac{D'^2 Z_C Z_m a_1 a_3 + D'(D' - K'D) Z_C Z_o}{D'^2 Z_C Z_m a_3^2 + (D' - K'D)^2 Z_C Z_o + Z_m Z_o a_2^2}. \tag{23}$$

In (23), a_1, a_2, and a_3 are the coefficients that considered in order to simplify the transfer functions and defined as follows:

$$a_1 = \frac{N_3 - N_2}{N_3}, \quad a_2 = \frac{N_1 + N_2}{N_3}, \quad a_3 = \frac{N_1 + N_3}{N_3}.$$

Substituting (15)–(17) into (23), we get the s-domain transfer function of G_{Vcv} as given by (24) shown at the bottom of the page.

B. Input Voltage to Output Voltage Transfer Function

Calculating $\hat{v}_m$ from (21) and substituting into (22), the following equation can be written:

$$\left(\frac{N_1 + N_3}{N_3}\right)\hat{v}_C - K'\left(1 + \frac{D}{D'}\right)\hat{v}_o - \hat{v}_{\text{in}} = 0. \tag{25}$$

Using (23) and (25), the input voltage to output voltage transfer function (G_{Vov}) can be calculated as follows:

$$G_{\text{Vov}} = \frac{\hat{v}_o}{\hat{v}_{\text{in}}}$$

$$= \frac{D'(D' - K'D) Z_C Z_o - D' a_1 a_2 Z_m Z_o}{D'^2 Z_C Z_m a_3^2 + (D' - K'D)^2 Z_C Z_o + Z_m Z_o a_2^2}. \tag{26}$$

Substituting (15)–(17) into (26), we get the s-domain transfer function of G_{Vov} as given by (27) shown at the bottom of the page.

$$G_{\text{Vcv}} = \frac{\hat{v}_C}{\hat{v}_{\text{in}}} = \frac{\left[D'^2 L_m a_1 a_3 + D'(D' - K'D) L_o\right] s + D'(D' - K'D) R_o}{(CL_m L_o a_2^2) s^3 + (CL_m R_o a_2^2) s^2 + \left[D'^2 L_m a_3^2 + (D' - K'D)^2 L_o\right] s + (D' - K'D)^2 R_o} \tag{24}$$

$$G_{\text{Vov}} = \frac{\hat{v}_o}{\hat{v}_{\text{in}}} = \frac{-(D'CL_m L_o a_1 a_2) s^3 - (D'CL_m R_o a_1 a_2) s^2 + D'(D' - K'D) L_o s + D'(D' - K'D) R_o}{(CL_m L_o a_2^2) s^3 + (CL_m R_o a_2^2) s^2 + \left[D'^2 L_m a_3^2 + (D' - K'D)^2 L_o\right] s + (D' - K'D)^2 R_o} \tag{27}$$

C. Input Voltage to Magnetizing Current Transfer Function

Using (19) and (20), the following equation can be written:

$$
\begin{aligned}
\frac{\hat{i}_m}{\hat{v}_C} = {} & \left(\frac{N_1 + N_2}{Z_C\, N_3}\right) \frac{D' + D}{D' - K'D} \\
& + \left(\frac{N_1 + N_3}{Z_o\, N_3}\right) \frac{D'}{D' - K'D}\left(\frac{\hat{v}_o}{\hat{v}_C}\right).
\end{aligned} \tag{28}
$$

Substituting from (21) into (28), a relation between the magnetizing current and capacitor voltage is achieved, and then using (23), the input voltage to magnetizing current transfer function (G_{iv}) can be calculated which is given by

$$
\begin{aligned}
G_{\mathrm{iv}} &= \frac{\hat{i}_m}{\hat{v}_{\mathrm{in}}} \\
&= \frac{D'^2 Z_C a_3 + D' Z_o a_2}{D'^2 Z_C Z_m a_3^2 + (D' - K'D)^2 Z_C Z_o + Z_m Z_o a_2^2}.
\end{aligned} \tag{29}
$$

Substituting (15)–(17) into (29), we get the s-domain transfer function of G_{iv} as given by (30) shown at the bottom of the page.

D. Control to Capacitor Voltage Transfer Function

In order to derive the transfer functions from control perturbation ($\hat{d}$), $\hat{v}_{\mathrm{in}}$ must be ignored in the ac small-signal model of PWM Y-source converter. As mentioned before, no perturbation is considered in load current. Hence, letting $\hat{v}_{\mathrm{in}} = 0$ and $\hat{i}_o = 0$ in Fig. 8, the ac small-signal model to derive control to capacitor voltage, output voltage, and magnetizing current transfer functions can be achieved like shown in Fig. 10. Using (18) and KCL in Fig. 10, the following equations can be written:

$$
\hat{i}_{\mathrm{in}} = \frac{\hat{i}_C + \hat{i}_o + K'\frac{I_{\mathrm{IN}}}{D'^2}\hat{d}}{1 - K'\frac{D}{D'}} \tag{31}
$$

$$
\hat{i}_m = \frac{N_2}{N_3}\hat{i}_C + \left(\frac{N_1}{N_3} + K'\frac{D}{D'}\right)\hat{i}_{\mathrm{in}} + K'\frac{I_{\mathrm{IN}}}{D'2}\hat{d} + \hat{i}_o. \tag{32}
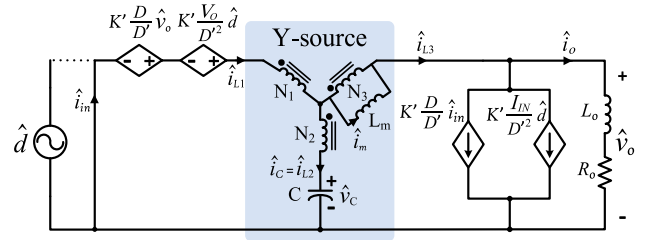$$

Fig. 10.   Ac small-signal model to derive control to capacitor voltage, output voltage and magnetizing current transfer functions.

Applying KVL on the left loop of the circuit in Fig. 10, the following equations can be written:

$$
\hat{v}_C + \left(\frac{N_1 + N_2}{N_3}\right)\hat{v}_m - K'\frac{D}{D'}\hat{v}_o - K'\frac{V_O}{D'^2}\hat{d} = 0. \tag{33}
$$

Considering Ohm's law for the voltage across magnetizing inductor, capacitor C, and output voltage, and using (21) and (31) into (33), the control to capacitor voltage transfer function (G_{Vcd}) can be derived in the impedance form which the simplified transfer function is given by (34) shown at the bottom of the page.

Substituting (15)–(17) into (34), we get the s-domain transfer function of G_{Vcd} as given by (35) shown at bottom of the page.

E. Control to Output Voltage Transfer Function

Calculating $\hat{v}_m$ from (21) and substituting into (33), the following equation can be written:

$$
K\hat{v}_C - K'\left(1 + \frac{D}{D'}\right)\hat{v}_o - K'\frac{V_O}{D'^2}\hat{d} = 0. \tag{36}
$$

Using (34) and (36), the control to output voltage transfer function (G_{Vod}) can be calculated, which is given by (37) shown at the bottom of the next page.

Substituting (15)–(17) into (37), we get the s-domain transfer function of G_{Vod} as given by (38) shown at the bottom of the next page.

$$
G_{\mathrm{iv}} = \frac{\hat{i}_m}{\hat{v}_{\mathrm{in}}} = \frac{D'CL_o a_2 s^2 + D'CR_o a_2 s + D'^2 a_3}{(\mathrm{CL}_m L_o a_2^2)\, s^3 + (\mathrm{CL}_m R_o a_2^2)\, s^2 + \left[D'^2 L_m a_3^2 + (D' - K'D)^2 L_o\right] s + (D' - K'D)^2 R_o} \tag{30}
$$

$$
G_{\mathrm{Vcd}} = \frac{\hat{v}_C}{\hat{d}} = \frac{K' Z_C V_O\left[(D' - K'D) Z_o + D' Z_m a_1 a_3\right] - Z_C Z_m Z_o I_{\mathrm{IN}} a_2 (D'K a_2 + DK' a_3)}{D'^3 Z_C Z_m a_3^2 + D'^2 Z_m Z_o a_2^2 + D'(D' - K'D)^2 Z_C Z_o + DD' Z_m Z_o K' a_1 a_2} \tag{34}
$$

$$
\begin{aligned}
G_{\mathrm{Vcd}} &= \frac{\hat{v}_C}{\hat{d}} \\
&= \frac{-\left[I_{\mathrm{IN}} L_m L_o a_2 (DK' a_3 + D'K a_2)\right] s^2 + \left[D'K'V_O L_m a_1 a_3 - I_{\mathrm{IN}} L_m R_o a_2 (DK' a_3 + D'K a_2) + (D' - K'D) K'V_O L_o\right] s + (D' - K'D) K'V_O R_o}{D'CL_m L_o a_2 (DK' a_1 + D' a_2) s^3 + D'CL_m R_o a_2 (DK' a_1 + D' a_2) s^2 + \left[D'^3 L_m a_3^2 + D'(D' - K'D)^2 L_o\right] s + D'(D' - K'D)^2 R_o}
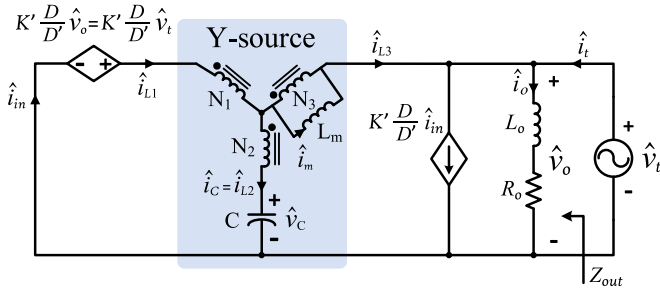\end{aligned} \tag{35}
$$

Fig. 11.   Ac small-signal model to derive output impedance transfer function.

F. Control to Magnetizing Current Transfer Function

Using (31) and (32), the following equation can be written:

$$\frac{\hat{i}_m}{\hat{v}_C} = \left(\frac{N_3 - N_2}{Z_C\,N_3}\right)\frac{D' + K'D}{D' - K'D} + \left(\frac{N_1 + N_3}{N_3}\right)\frac{K'\frac{I_{\text{IN}}}{D'}}{D' - K'D}$$

$$\times \left(\frac{\hat{d}}{\hat{v}_C}\right) + \left(\frac{N_1 + N_3}{Z_o\,N_3}\right)\frac{D'}{D' - K'D}\left(\frac{\hat{v}_o}{\hat{v}_C}\right). \quad (39)$$

Using (33) and substituting from (34) into (39), the control to magnetizing current transfer function (G_{id}) can be calculated, which the simplified transfer function is given by (40) shown at the bottom of the page.

Substituting (15)–(17) into (34), we get the *s*-domain transfer function of G_{id} as given by (41) shown at the bottom of the page.

G. Open-Loop Input and Output Impedances

The small-signal equivalent circuit shown in Fig. 9 can be used to derive open-loop input impedance transfer function of the PWM Y-source converter. Considering Ohm's law for the voltage across capacitor C and output voltage, and using (19), the following equation can be written:

$$\frac{\hat{v}_{\text{in}}}{\hat{i}_{\text{in}}} = \frac{1 - K'\frac{D}{D'}}{\frac{1}{\hat{v}_{\text{in}}}\left(\frac{\hat{v}_C}{Z_C} + \frac{\hat{v}_o}{Z_o}\right)} \quad (42)$$

Substituting from (23) and (26) into (42), the open-loop input impedance of the PWM Y-source converter can be obtained, which is given by (43) shown at the bottom of the next page.

Substituting (15)–(17) into (43), we get the *s*-domain transfer function of the input impedance as given by (44) shown at the bottom of the next page.

In order to derive open-loop output impedance transfer function of the PWM Y-source converter, all perturbation signals must be ignored. Hence, letting $\hat{v}_{\text{in}} = 0$, $\hat{d} = 0$, and $\hat{i}_o = 0$ in Fig. 8 and using a test voltage $\hat{v}_t$ with a current of $\hat{i}_t$ at the output of the model lead to the ac small-signal model to derive output impedance of the PWM Y-source converter which is given in Fig. 11. From Fig. 11, applying KCL and using (18), the following equations can be written:

$$\hat{i}_{\text{in}} = \frac{\hat{i}_C + \hat{i}_o - \hat{i}_t}{1 - K'\frac{D}{D'}} \quad (45)$$

$$\hat{i}_m = \frac{N_2}{N_3}\hat{i}_C + \left(\frac{N_1}{N_3} + K'\frac{D}{D'}\right)\hat{i}_{\text{in}} + \hat{i}_o - \hat{i}_t. \quad (46)$$

Applying KVL on the outer and left loops of the circuit in Fig. 11, the following equations can be written:

$$\left(\frac{N_1 + N_3}{N_3}\right)\hat{v}_m + \left(1 - K'\frac{D}{D'}\right)\hat{v}_t = 0 \quad (47)$$

$$\left(\frac{N_1 + N_2}{N_3}\right)\hat{v}_m + \hat{v}_C - K'\frac{D}{D'}\hat{v}_t = 0. \quad (48)$$

Substituting (45) into (46) and considering Ohm's law for the voltage across magnetizing inductor, capacitor C, and output voltage, and using (47) and (48), the output impedance transfer function can be achieved, which is equal to the ratio of the test voltage over its current

$$Z_{\text{out}} = \frac{\hat{v}_t}{\hat{i}_t}$$

$$= \frac{D'^2 Z_C Z_m Z_o a_3^2}{D'^2 Z_C Z_m a_3^2 + (D' - K'D)^2 Z_C Z_o + Z_m Z_o a_2^2}. \quad (49)$$

Substituting (15)–(17) into (49), we get the *s*-domain transfer function of the output impedance as given by (50) shown at the bottom of the next page.

$$G_{\text{Vod}} = \frac{\hat{v}_o}{\hat{d}} = \frac{K'Z_o V_O\left[(D' - K'D)Z_C - Z_m a_1 a_2\right] - Z_C Z_m Z_o I_{IN} a_2 D'\left(Ka_2 + a_3\right)}{D'^3 Z_C Z_m a_3^2 + D'^2 Z_m Z_o a_2^2 + D'\left(D' - K'D\right)^2 Z_C Z_o + D D' Z_m Z_o K' a_1 a_2}. \quad (37)$$

$$G_{\text{Vod}} = \frac{\hat{v}_o}{\hat{d}}$$

$$= \frac{-\left(K'V_O C L_m L_o a_1 a_2\right)s^3 - \left[K'V_O C L_m R_o a_1 a_2 + D'I_{IN} L_m L_o a_2 (a_3 + Ka_2)\right]s^2 + \left[K'V_O L_o\left(D' - K'D\right) - D'I_{IN} L_m R_o a_2 (a_3 + Ka_2)\right]s + K'V_O R_o\left(D' - K'D\right)}{D'C L_m L_o a_2\left(DK'a_1 + D'a_2\right)s^3 + D'C L_m R_o a_2\left(DK'a_1 + D'a_2\right)s^2 + \left[D'^3 L_m a_3^2 + D'(D' - K'D)^2 L_o\right]s + D'(D' - K'D)^2 R_o} \quad (38)$$

$$G_{\text{id}} = \frac{\hat{i}_m}{\hat{d}} = \frac{K'V_O\left(D'Z_C a_3 + Z_o a_2\right) + \left(D' - K'D\right)K'Z_C Z_o I_{IN} a_3}{D'^3 Z_C Z_m a_3^2 + D'^2 Z_m Z_o a_2^2 + D'\left(D' - K'D\right)^2 Z_C Z_o + D D' Z_m Z_o K' a_1 a_2}. \quad (40)$$

$$G_{\text{id}} = \frac{\hat{i}_m}{\hat{d}} = \frac{K'V_O C L_o a_2 s^2 + K'\left[V_O C R_o a_2 + \left(D' - K'D\right)I_{IN} L_o a_3\right]s + D'K'a_3\left[V_O + \left(D' - K'D\right)I_{IN} R_o\right]}{D'C L_m L_o a_2\left(DK'a_1 + D'a_2\right)s^3 + D'C L_m R_o a_2\left(DK'a_1 + D'a_2\right)s^2 + \left[D'^3 L_m a_3^2 + D'\left(D' - K'D\right)^2 L_o\right]s + D'\left(D' - K'D\right)^2 R_o} \quad (41)$$

IV. MODEL AND TRANSFER FUNCTION VALIDATIONS

In this section, some computer simulations have been done using MATLAB software to both verify and compare the frequency and dynamic responses of the PWM MCIS converters. To evaluate the effectiveness of the generalized transfer functions of the PWM Y-source converter, all predicted theoretical responses are carried out using the transfer functions of the PWM Y-source converter. As mentioned before and like the illustration in Fig. 3, by letting $N_1 = 0$ all transfer functions change for PWM Γ-source converter and by letting $N_2 = 0$ all transfer functions change for PWM T-source converter. Furthermore, to change the linear model of the PWM Y-source converter for the PWM Γ-source and PWM T-source converters, in addition to the replacement of impedance networks, the winding coefficient K' in any equation and ac small-signal models of the PWM Y-source converter should be replaced with the related winding coefficients of Γ-source and T-source. The relation between the winding coefficient of Y-source and the turns ratios of Γ-source and T-source are as follows:

$$K' = \frac{1}{n_\Gamma - 1} = n_T. \tag{51}$$

In (35), $n_\Gamma = N_3/N_2$ and $n_T = N_1/N_3$ are the turns ratios for Γ-source and T-source, respectively. Substituting the turns ratios into (51) and considering Fig. 3, the transition between MCISs will become more apparent as written in

$$\left[\frac{N_1 + N_2}{N_3 - N_2}\right]_Y = \left[\frac{N_2}{N_3 - N_2}\right]_\Gamma = \left[\frac{N_1 + N_3}{N_3}\right]_T. \tag{52}$$

The parameters used in computer simulations through the paper are listed in Table II. The winding factor (K) for all three networks is assumed to be about 4, consequently there would be $K' = 3$ for Y-source, $n_\Gamma = 4/3$ for Γ-source, and $n_T = 3$ for T-source. Moreover, with respect to the assumed turns ratios, the related winding turns $(N_1 : N_2 : N_3)$ for the networks are as follows: (1:2:3) for Y-source, (0:3:4) for Γ-source, and (3:0:1) for T-source. In order to conduct a fair assessment, an identical total inductance (L) and total parasitic resistance (ESR$_T$) of all windings is considered for Y-source, Γ-source, and T-source, which means that the amount of wire used for all coupled inductors are identical. In the computer simulations through the paper, a 1.2-mH total inductance and a 1-Ω total parasitic resistance are

TABLE II
SIMULATION PARAMETERS OF MCIS CONVERTERS

Parameters	Values
Input voltage (V_{IN})	15 V
Winding factor (K)	4
Duty cycle (D)	0.08
Load	40 Ω, 2.3 mH
Capacitor (C)	470 μF
Series resistance of C (ESR$_C$)	85 mΩ
Total inductance (L)	1.2 mH
Total parasitic resistance (ESR$_T$)	1 Ω
Switching frequency (f_s)	25 kHz

considered for all networks, then its per unit (PU) value from the third winding (N_3) can be used as the magnetizing impedance (Z_m) and ESR$_L$ of the transfer functions. Since, including circuit parasitic series resistances tend to reduce the nonminimum phase (NMP) effect and to decelerate the system dynamics [27], [28]; in order to effectively observe and compare the dynamic and frequency responses of the three mentioned MCIS converters, the ESRs are neglected in this section and a 10-Ω resistive load is considered for all MCIS converters.

A. Dynamic Response Validation

To verify the dynamic behavior of the averaged large signal circuit models, the detailed circuit (see Fig. 2) and the averaged circuit models (see Fig. 5) of all three PWM Y-source, Γ-source, and T-source converters have been implemented in MATLAB/Simulink software. In the first case, a step change in input voltage (V_{IN}) from 15 to 20 V is applied at the time $t = 0.1$ (s) of the simulations and the results for all converters are shown in Fig. 12. As indicated in the plots, the blue lines are the response of detailed circuit model of all PWM MCIS converters in Simulink software and the red lines are the response of the related transfer functions G_{Vcv}, G_{Vov}, and G_{iv}, in the left, middle, and right columns of Fig. 12, respectively.

In the second case, a step change in duty cycle (D) from 0.1 to 0.15 is applied at the time $t = 0.1$ (s) of the simulations and the results for all converters are shown in Fig. 13. Dynamic response of capacitor voltage, output voltage, and magnetizing current are shown in blue color and the averaged model responses are shown in red color for G_{Vcd}, G_{Vod}, and G_{id},

$$Z_{in} = \frac{\hat{v}_{in}}{\hat{i}_{in}} = \frac{(D' - K'D)\left[Z_m Z_o a_2 (a_2 D' + a_1 K'D) + D'^2 Z_C Z_m a_3^2 + Z_C Z_o (D' - K'D)^2\right]}{D'^2 (D' - K'D)(Z_C + Z_o) + D'^2 Z_m a_1 (D'a_3 - a_2)} \tag{43}$$

$$Z_{in} = \frac{\hat{v}_{in}}{\hat{i}_{in}}$$

$$= \frac{[(D' - K'D)CL_m L_o a_2 (DK'a_1 + D'a_2)]s^3 + [(D' - K'D)CL_m R_o a_2 (DK'a_1 + D'a_2)]s^2 + \left[(D' - K'D)^3 L_o + D'^2 (D' - K'D)L_m a_3^2\right]s + (D' - K'D)^3 R_o}{[D'^2 (D' - K'D)CL_o + D'^2 CL_m a_1 (D'a_3 - a_2)]s^2 + [D'^2 (D' - K'D)CR_o]s + D'^2 (D' - K'D)} \tag{44}$$

$$Z_{out} = \frac{\hat{v}_t}{\hat{i}_t} = \frac{D'^2 L_m L_o a_3^2 s^2 + D'^2 L_m R_o a_3^2 s}{CL_m L_o a_2^2 s^3 + CL_m R_o a_2^2 s^2 + \left[D'^2 L_m a_3^2 + (D' - K'D)^2 L_o\right]s + (D' - K'D)^2 R_o} \tag{50}$$
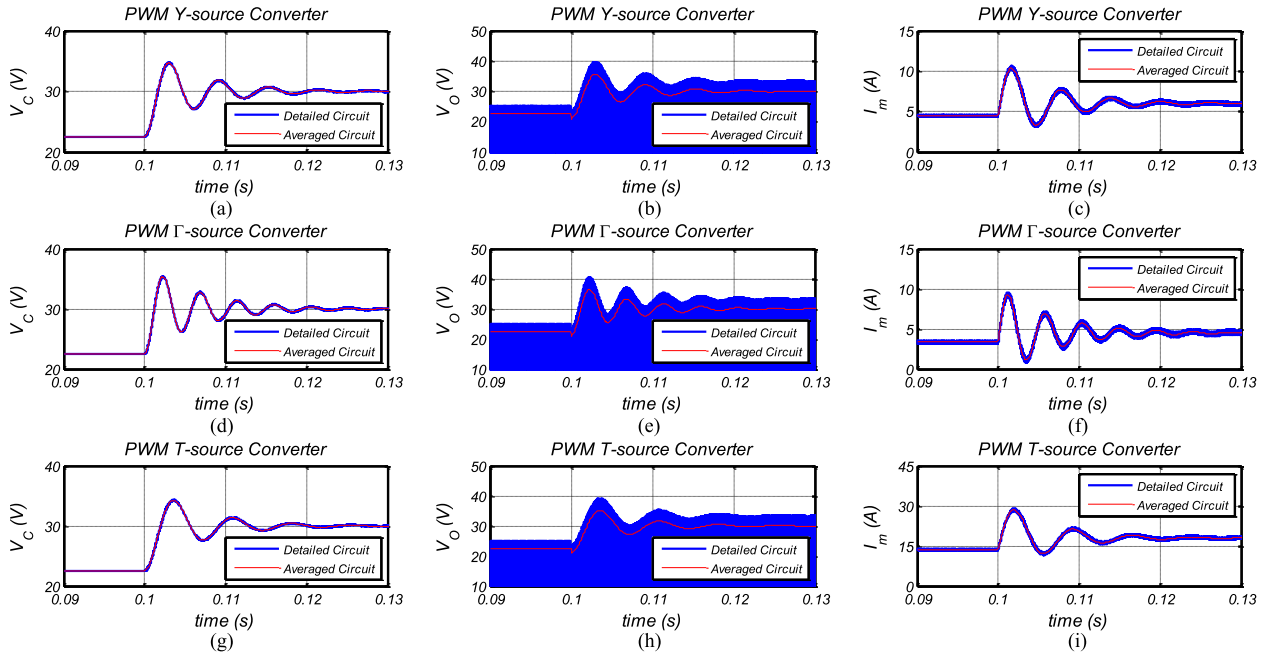
Fig. 12. Dynamic response of the PWM MCIS converters with increase in their input voltage (V_{in}) from 15 to 20 V ($D = 0.1$, $R = 10\ \Omega$).
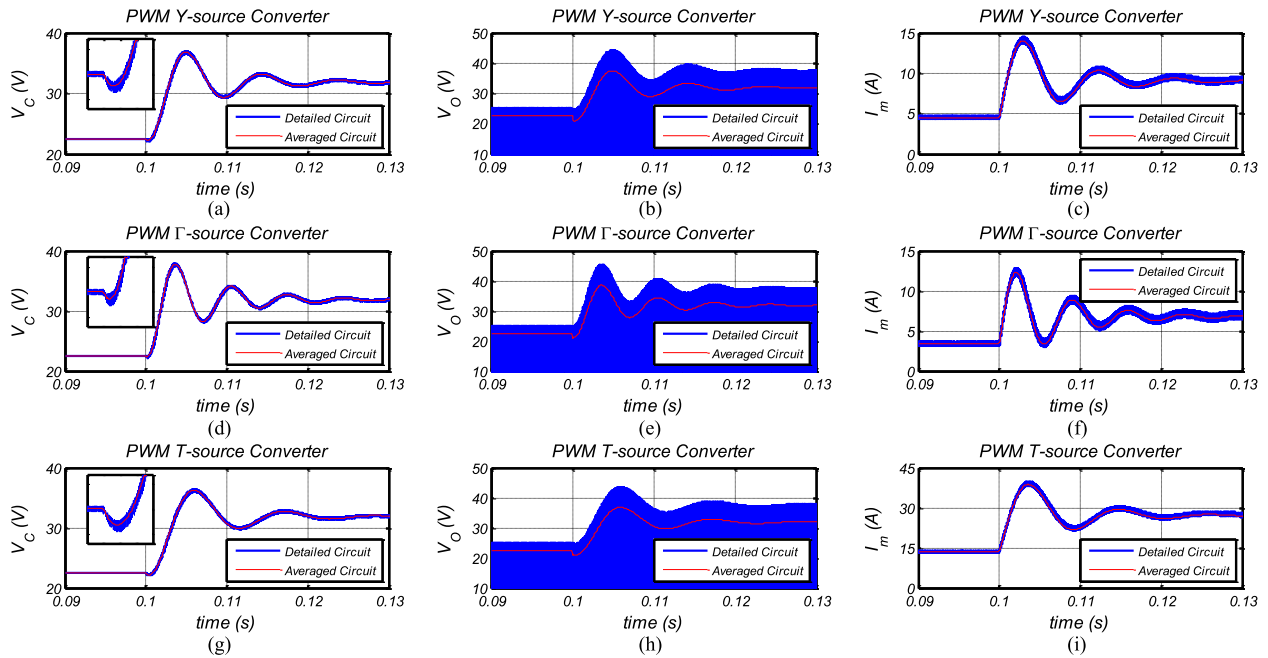

Fig. 13. Dynamic response of the PWM MCIS converters with increase in their duty cycle (D) from 0.1 to 0.15 ($V_{in} = 15$ V, $R = 10\ \Omega$).

in the left, middle, and right columns of Fig. 13, respectively. Evidently, the dynamic responses of all three PWM MCIS converters are in well agreement with their large small averaged model responses. A small difference between the amplitude of the output voltage of circuit and averaged models can be seen in both Figs. 12 and 13. This is because the output of PWM MCIS converters is pulsating and the peak of the output voltage has a linear relation (V_O (peak) $= V_O/D'$) with the averaged model response.

In the dynamic response of the capacitor voltage (V_C) to a step change in D, an undershoot can be seen before V_C rises. Same as reported in the literature for the Z-source converter [14], [15], this phenomena is because of the right half-plane (RHP) zero of the control to capacitor voltage transfer function (G_{Vcd}). Moreover, a voltage dip can be seen in the output voltage dynamics, which is related to the RHP zero in its input and control to output voltage transfer functions (G_{Vov} and G_{Vod}). The mentioned behavior is a typical nature for a

NMP system, in which the system tends to move in opposite direction at the initiation of any disturbances. Typically, the NMP effect of the MCIS converters makes the design of a closed-loop system more difficult for control designers [29]. Additionally, from (26) and (38)), it can be seen that both output transfer functions are semiproper, which makes controller design difficult. Comparing Fig. 13(a), (d), and (g), it can be inferred that the Γ-source converter has a low NMP undershoot which leads to a more convenient closed-loop controller design than two other PWM converters. According to Figs. 12 and 13, it is obvious that the overshoot in capacitor voltage in the Γ-source converter is higher than in two other converters. In addition, the PWM T-source converter has the highest damping and the PWM Γ-source converter has the lowest damping between the mentioned PWM MCIS converters. Same behaviors can be observed for output voltage and magnetizing current.

B. Frequency Response Validation

In order to evaluate the validity of the derived transfer functions, the linear small-signal model of the PWM MCIS converters are implemented in Simulink software. The frequency response of each converter is evaluated by the respective transfer function from the PWM Y-source converter. The ac small-signal model to derive input voltage to capacitor voltage, output voltage, and magnetizing current of the PWM Y-source converter, which is illustrated in Fig. 9, have been implemented in Simulink. According to the illustration in Fig. 3, in order to achieve the related frequency responses for the PWM Γ-source and T-source converters, only the impedance network of Fig. 9 must be changed in the Simulink model. Furthermore, to obtain the frequency response with perturbation in duty cycle, the ac small-signal model to derive control to capacitor voltage, output voltage, and magnetizing current of the PWM Y-source converter, which is illustrated in Fig. 10, have been implemented in Simulink. Fig. 14 depicts the frequency response for the transfer functions G_{Vcv}, G_{Vcd}, G_{Vov}, G_{Vod}, G_{iv}, and G_{id} along with their frequency responses from the Simulink linear models of the mentioned PWM MCIS converters.

Because all simulation parameters for PWM MCIS converters are same, the only parameter that affects the frequency responses are different PU magnetizing inductance on the third winding of the MCISs. By letting an identical total inductance for all mentioned MCISs, the effect of turns ratios is diminished but it is more equitable from the circuit design viewpoint. From Fig. 14, it can be seen that the PWM Γ-source converter generally has a high corner frequency, which causes to a higher rise time in compared with two other PWM converters. Furthermore, in term of capacitor or output voltage transfer functions, it can be inferred that the Γ-source has a high magnitude peak, which causes to a higher overshoot in compared with two other PWM converters. Moreover, in terms of magnetizing current transfer functions, the T-source has a high magnitude peak, which causes to a higher overshoot in compared with two other PWM converters. Regarding the stability margin of these converters, there is no clear difference in the phase margin (PM) of control to capacitor voltage, output voltage, and magnetizing current transfer functions. However, in the input to capacitor voltage and magnetizing current transfer functions, it can be seen that

the PWM Y-source converter has higher PM than two other PWM converters.

To verify the open-loop input and output impedances, the ac small-signal models given in Figs. 9 and 11 have been implemented in Simulink software, respectively. The simulated and theoretical transfer functions from the derived impedances are shown in Fig. 15. It is evident that same phenomena as in capacitor and output voltage transfer functions can be seen for the magnitude peak and break frequency of impedance transfer functions of PWM MCIS converters.

In order to summarize the salient features of the MCIS converter, a summary of dynamic and stability characteristics of the PWM MCIS converters is drawn in Table III. It should be mentioned that both dynamic and stability characteristics of the PWM Y-source converter are dependent to its various windings combinations. Hence, it is not applicable to have a general decision for the behavior of the Y-source converter with all windings combinations. In the next section, the impact of various parameters on both dynamic and stability of the MCIS converters are investigated in detail. Furthermore, the effect of ESR of the capacitor C on the stability margin of the mentioned systems is studied via z plane analysis and bode plots.

V. COMPREHENSIVE ANALYSIS OF FREQUENCY RESPONSE AND STABILITY MARGIN FOR VARIOUS MCIS NETWORKS

In order to understand the effect of parameter variations on the transfer functions of the PWM MCIS converters, the placement of poles and zeros are assessed in this section. In the impedance-source-based converters, the control to capacitor voltage transfer function (G_{Vcd}) is one of the most important and challenging transfer functions that should be taken care of. Hence, in order to design an stable control loop for such NMP system like G_{Vcd}, the effects of parameters variation should be thoroughly investigated for the system. In addition, in the last part of this section, a comparative study on the stability margin of G_{Vcv} for PWM MCIS converters is presented.

A. Impact of Capacitance and Inductance

In this section, the pole and zero trajectories with total inductance (L) and capacitance (C) variations for the PWM Y-source converter have been evaluated. It should be noted that by including the ESR of capacitor, an additional left half-plane zero appears in the control to capacitor voltage transfer function (G_{Vcd}), which in the following illustrations are marked with "From ESR$_C$." According to Fig. 16(a), apparently the RHP zero moves toward the origin with the increase of total inductance, which makes the NMP phase effect of G_{Vcd} to be more severe. Considerably, variation in L leads to a significant change on the placements of the RHP zero and conjugate pole pairs. On the other hand, variation in capacitance has no effect on the RHP zero and mostly affects system poles than zeros. However, the ESR$_C$ zero is an exception, which by increase in capacitance the ESR$_C$ zero moves toward the origin. Regarding conjugate pole pairs, the effect of increasing L leads to increased damping factor and settling time, and the effect of increasing C leads to increased oscillatory response and decreased settling
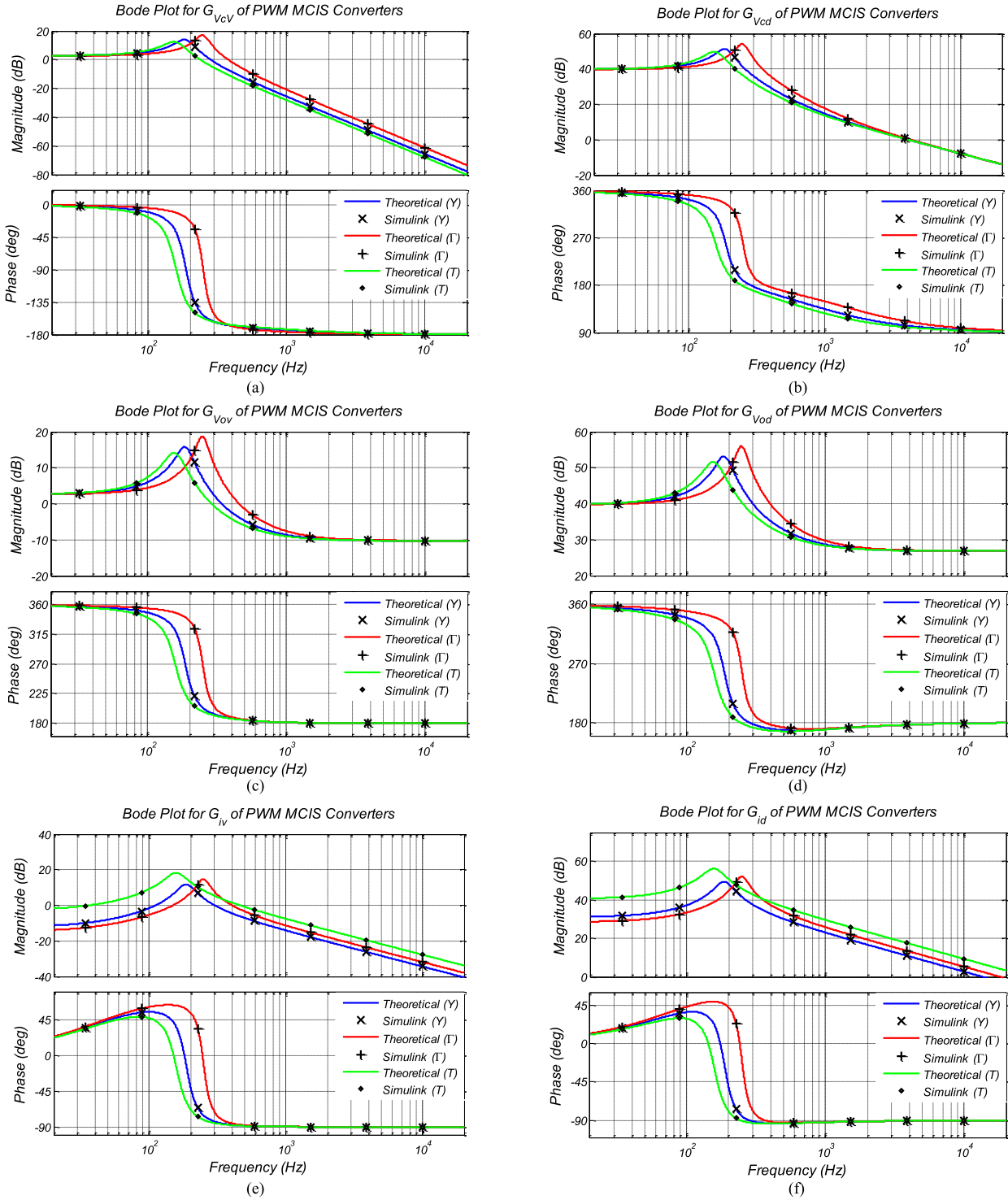
Fig. 14. Frequency response of the PWM MCIS converters for all derived transfer functions ($G_{\text{Vcv}}/G_{\text{Vcd}}$, $G_{\text{Vov}}/G_{\text{Vod}}$, and $G_{\text{iv}}/G_{\text{id}}$).

time. In addition, increasing C moves the real pole away from the imaginary axis, which leads to reduced damping effect. On the other hand, increasing L has low effects on real pole/zero placements. It should be noted that same effects have been observed on two other PWM MCIS converters, and, hence, are not shown in the paper. In overall, inductance and capacitance values must be chosen with respect to various desired tradeoffs,

such as ripple performance, cost and size, damping factor, and stability margin.

B. Impact of Winding Factor (Turns Ratio) and Duty Cycle

In this section, the effects of variation in duty cycle and turns ratios have been evaluated. The effect of duty cycle variation on PWM Y-source converter with $K = 4$ is drawn in Fig. 17(a).
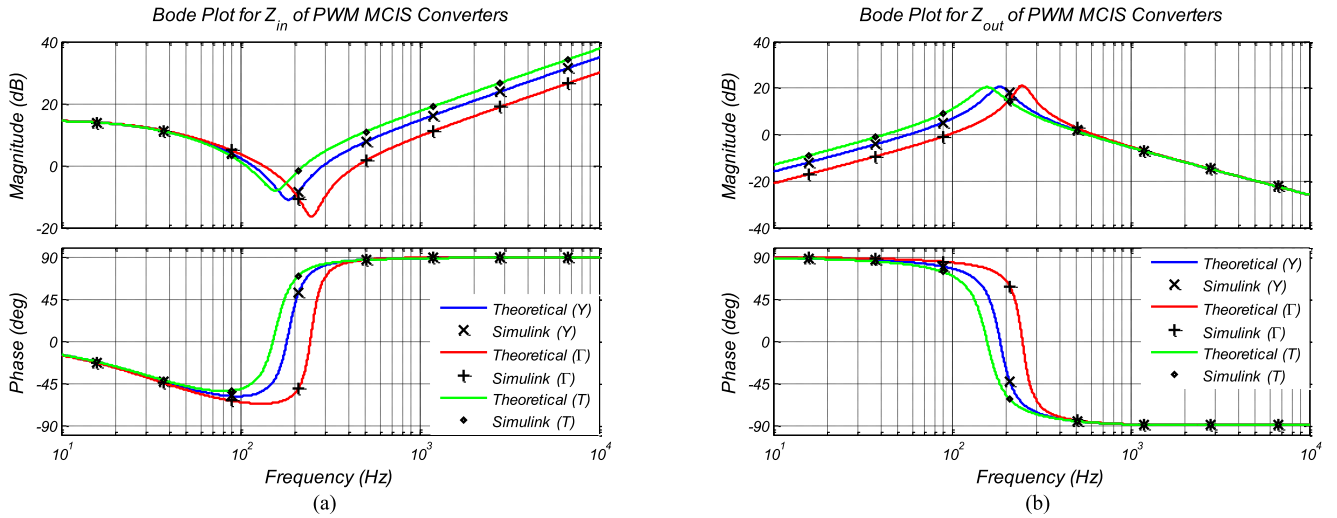
Fig. 15.   Frequency response for the open-loop input and output impedances of the PWM MCIS converters.

TABLE III
DYNAMIC AND STABILITY CHARACTERISTICS OF PWM MCIS CONVERTERS

	PWM Y-source	PWM Γ-source	PWM T-source
System dynamic and stability characteristics	• Moderate damping • Moderate NMP undershoot • Moderate oscillatory response • Low settling time • Low natural frequency	• High settling time • High oscillatory response • High natural frequency • Low damping • Low NMP undershoot	• High damping • High NMP undershoot • Low oscillatory response • Low settling time • Low natural frequency

It can be inferred that in high duty cycles near to maximum allowable duty cycle ($D_{\max} = 1/4$), the RHP zero is very close to the origin, and, hence, the NMP phase effect of the G_{Vcd} enhances significantly, which leads the system toward instability and severe closed-loop control design. The same effect observed on two other PWM MCIS converters. Fig. 17(b) shows the effect of increasing the winding factor of the PWM Y-source converter. As can be seen a similar impact as duty cycle variation is observed by increase in the winding factor and turns ratios of the MCIS converters.

By increasing the duty cycle or the turns ratios of the PWM MCIS converters, the conjugate pole pairs move toward the real axis, while the RHP zero moves toward the origin. However, the system damping increases by moving conjugate pole pairs toward the real axis, but presence of the RHP zero diminishes system damping effect and slows down the system transient response. Hence, the system settling time increases by the increasing of duty cycle or turns ratios.

In fact, increasing duty cycle or winding ratio separately leads to the increased voltage gain of those MCIS converters, which correspond to the increased power level. In order to better understand the effect of duty cycle and turns ratio along together and neglecting load effects, the pole and zero trajectories are drawn for the PWM Y-source converter with a specific voltage gain (M = V_O/V_{IN} = 2) and various winding factors (K) and

duty cycles. Fig. 17(c) shows the effect of increasing K with a constant voltage gain. Clearly, the NMP effect of G_{Vcd} increases by selecting a high winding factor. Similar phenomena have been observed for the PWM Γ-source and T-source converters with a low n_Γ and a high n_T, respectively, which due to brevity have not shown in the paper. Consequently, in order to facilitate controller design, it is essential to select appropriate winding ratios on MCIS converters.

C. Impact of Load Resistance

In order to assess the effect of load change in the dynamic and stability of the MCIS converters, some simulations have been done using the aforementioned parameters with a 5—40-Ω load variation and consequent results are shown in Fig. 18. Indeed, increasing the load resistance moves the conjugate pole pairs toward both the real and imaginary axes and the real pole/zero and RHP zero away from the imaginary axis. This generally leads to an increased settling time, system damping, and decreased NMP effect natural frequency. In addition, increasing load resistance moves the conjugate pole pairs very near to the imaginary axis, which, in general, affects system damping and oscillatory response. It can be seen that the more the load current increases (which correspond to the lower Ro), the more the real pole approaches to the origin. In this case, after a specific load resistance the real pole will be dominant as depicted in Fig. 18(a). Regarding the stability margin, increasing the load resistance (which correspond to the lower load current) tends the system to an increased stability. This can be inferred from both the placement of RHP zeros as shown in Fig. 18(a) and the frequency response of the PWM MCIS converters as depicted in Fig. 18(b).

D. Impact of ESRs on Stability Criteria

The effect of variation in parasitic parameters of the magnetizing inductor (ESR_L) and capacitor (ESR_C) is taken into account in this section. Fig. 19(a) shows the effect of increase in the ESR_L in the pole and zero placements. With the increase
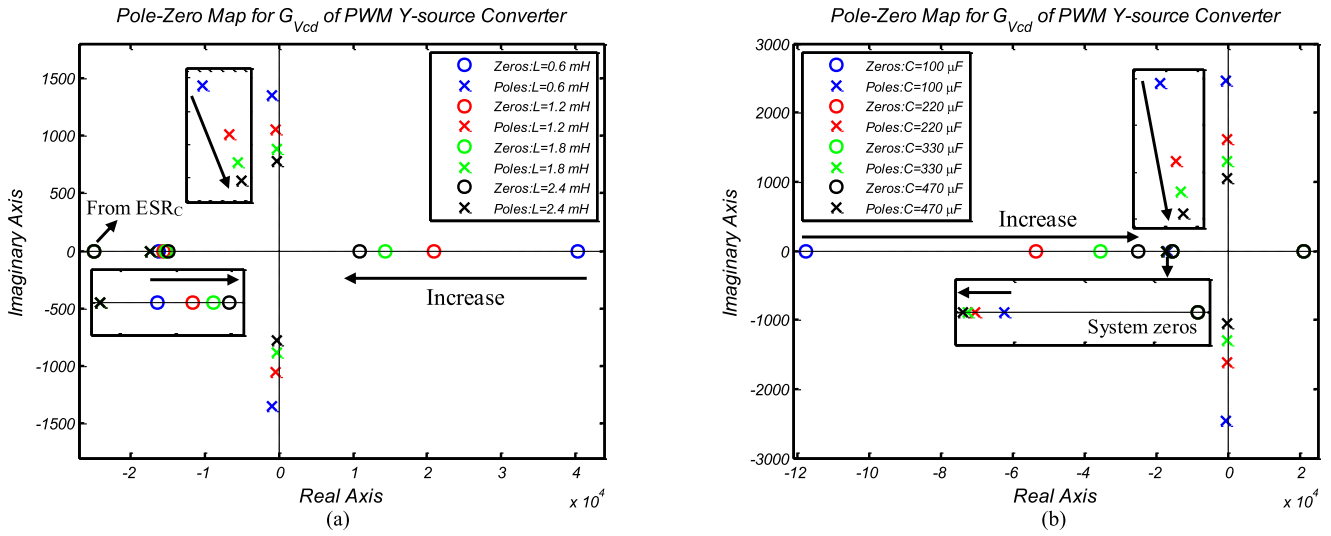
Fig. 16. Pole and zero map for G_{Vcd} with (a) inductance and (b) capacitance variations for PWM Y-source converter.
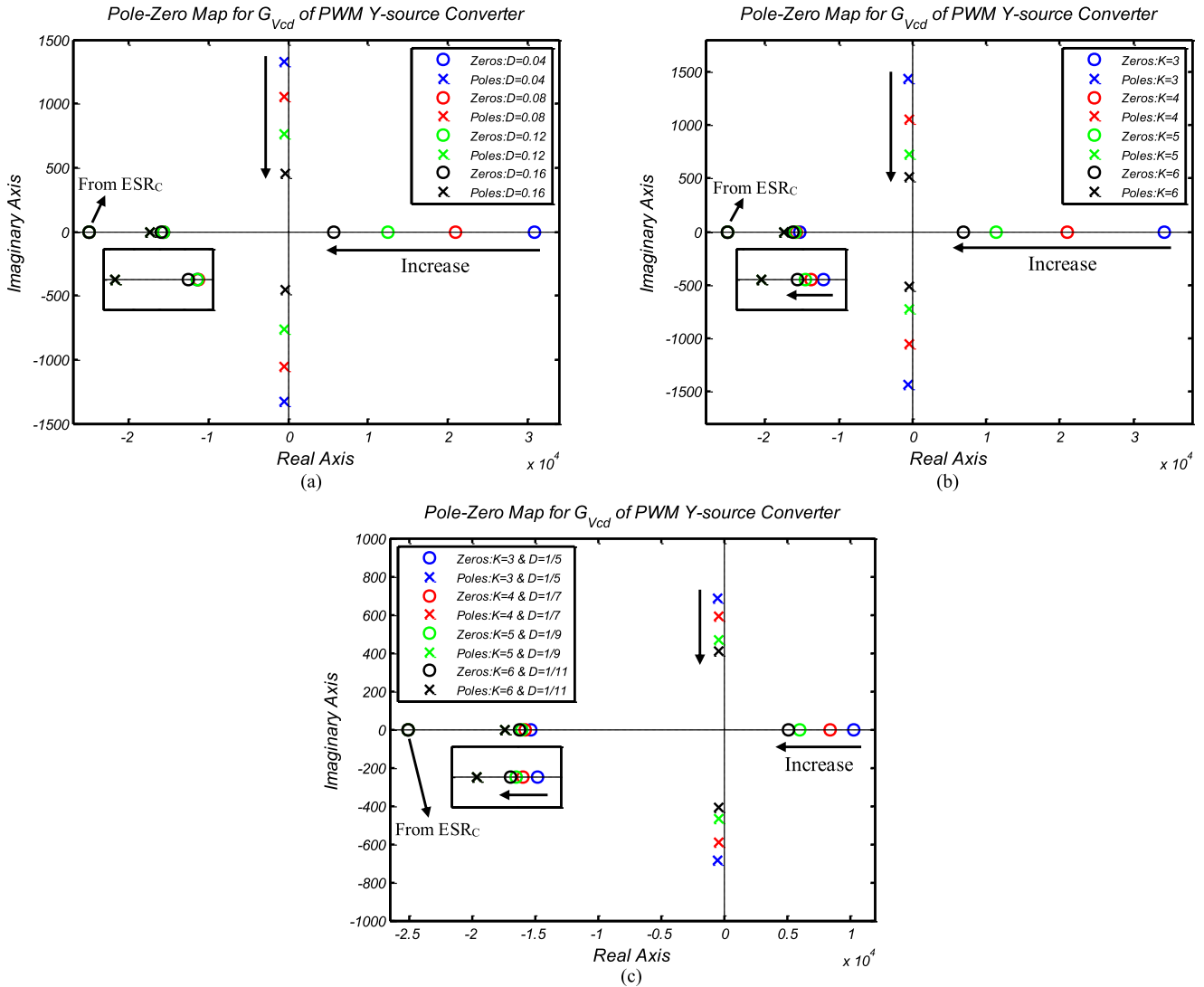

Fig. 17. Pole and zero map of G_{Vcd} (a) with variation in duty cycle and (b) with variation in winding factor, and (c) with variation in both duty cycle and winding factor with a constant voltage gain ($M = 2$).
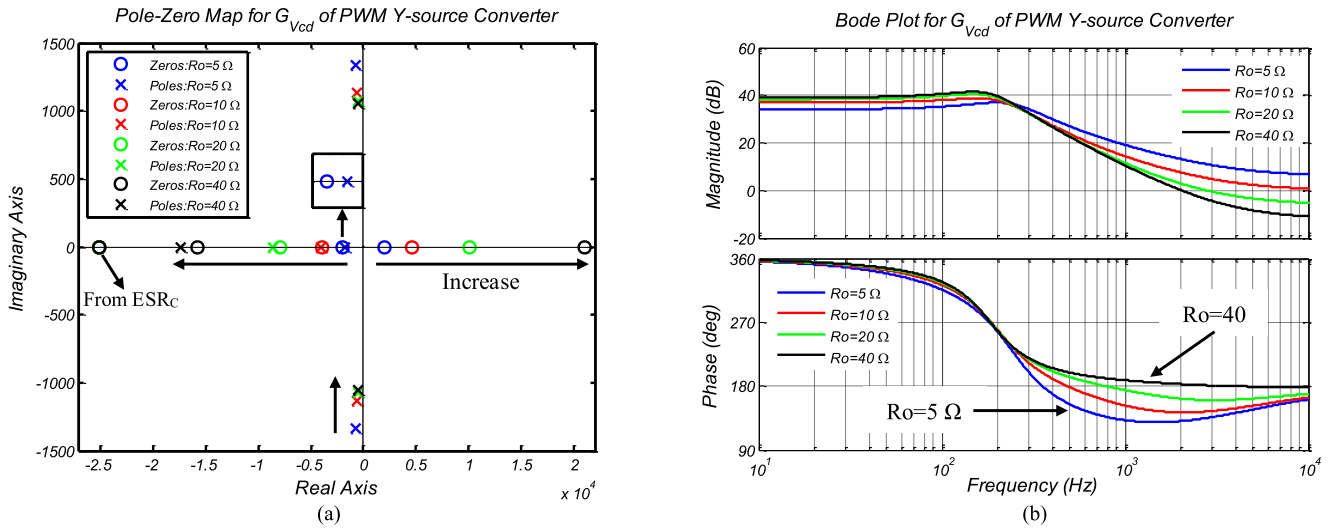
Fig. 18.	(a) Pole and zero map and (b) bode plot of G_{vd} over wide range of load variations (5–40 Ω).
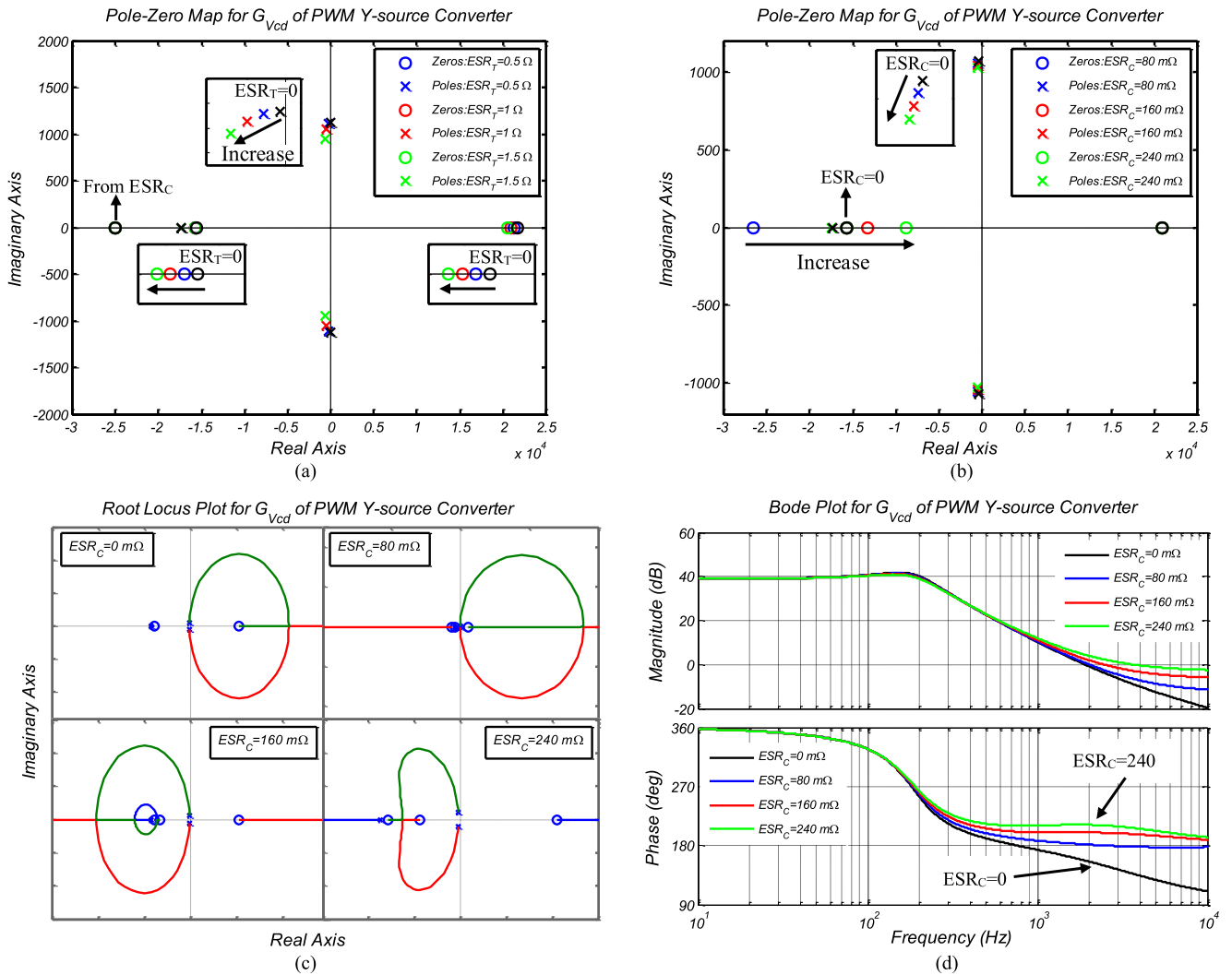

Fig. 19.	(a) Pole-zero map with variation in $\mathrm{ESR_L}$, (b) with variation in $\mathrm{ESR_C}$, (c) root locus, and (d) bode plots for G_{Vcd} with variation in $\mathrm{ESR_C}$.

TABLE IV
SUMMARY OF THE IMPACT OF PARAMETER VARIATIONS ON THE MCIS CONVERTERS DYNAMICS

Parameter	Change	Effect on Position of				Impact on System Dynamics and Stability
		Conjugate Poles	Real Pole	Real Zero	RHP Zero	
Total inductance (L)	Increase	Move toward the real axis	Move toward the imaginary axis	Move toward the imaginary axis	Move toward the imaginary axis	• Increase NMP effect • Restrict controller design • Increase rise time • Increase damping factor • Decrease oscillatory response • Decrease natural frequency
Capacitance (C)	Increase	Move toward the real axis and the imaginary axis	Move away from the imaginary axis	Constant	Constant	• Increase rise time • Increase settling time • Increase oscillatory response • Decrease damping factor • Decrease NMP undershoot • Decrease natural frequency
Shoot-through duty cycle (D)	Increase	Move toward the real axis	Not significant	Not significant	Move toward the imaginary axis	• Increase NMP effect • Restrict controller design • Increase rise time • Increase settling time • Increase system damping • Decrease natural frequency
Winding factor for Y-source (K)	Increase	Move toward the real axis	Not significant	Not significant	Move toward the imaginary axis	• Increase NMP effect • Restrict controller design • Increase rise time • Increase settling time • Increase system damping • Decrease natural frequency
Turns ratio for Γ-source (n_Γ)	Decrease					
Turns ratio for T-source (n_T)	Increase					
Load Resistance (R$_O$)	Increase	Move toward the real axis and the imaginary axis	Move away from the imaginary axis	Move away from the imaginary axis	Move away from the imaginary axis	• Increase settling time • Facilitate controller design • Increase oscillatory response • Decrease NMP effect • Decrease natural frequency
ESR of magnetizing inductor (ESR$_L$)	Increase	Move toward the imaginary axis and away from the real axis	Move away from the imaginary axis	Move away from the imaginary axis	Move toward the imaginary axis	• Increase NMP effect • Restrict controller design • Increase system damping • Increase voltage ripple across L • Decrease settling time • Decrease boost capability
ESR of capacitor (ESR$_C$)	Increase	Move toward the imaginary axis and away from the real axis	Move away from the imaginary axis	Constant	Constant	• Facilitate controller design • Increase system damping • Increase current ripple through C • Decrease settling time • Decrease oscillatory response • Decrease boost capability

of ESR$_L$, the RHP zero moves toward the origin, which has a negative effect on the closed-loop control design. In addition, conjugate pole pairs move away from the imaginary axis and toward the real axis, which raises damping effect and reduces oscillatory response of the system. It is clear that the variation in ESR$_L$ has a low influence on the real pole/zero placements.

In Fig. 19(b), the zero that is marked with ESR$_C$ = 0 and the RHP zeros are coincided natural zeros of G_{Vcd} that remained unchanged and the other moving zeros are additional zeros related to the ESR of capacitor. Moreover, variation of ESR$_C$ has a slight effect of the system poles and damping factor that shown in Fig. 19(b). Regarding to the placement of the ESR$_C$ zero, the root locus plot of the G_{Vcd} varies as shown in Fig. 19(c). If the additional zero places somewhere more far away from imaginary axis than the real pole does, the system is unstable. Otherwise, if the additional zero places somewhere more toward the imaginary axis than the real pole does, the system achieves a minimum stability margin.

Indeed, the mentioned phenomena can be inferred from bode plot of PWM Y-source converter with different ESR$_C$. In Fig. 19(d), the system is unstable with ESR$_C$ = 0 and by increasing the value of ESR$_C$, the system move toward stability where with ESR$_C$ = 160 mΩ and ESR$_C$ = 240 mΩ, the system gain a minimum PM. In practice, utilizing of zero ESR capacitors in impedance-source-based converters can lead the closed-loop system to instability. Same phenomenon reported in [30] for the buck converter. On the other hand, a large ESR value has a diminishing effect on the voltage boosting of MCIS converters. Subsequently, the ESR of capacitor should be chosen with respect to as low as power loss along with achieving a minimum system stability. Moreover, the minimum ESR of capacitor for the PWM MCIS converters can be selected regarding to other system parameters that place the real pole of G_{Vcd}.

The effect of poles and zeros placement in the dynamics of MCIS converters has been depicted and argued in three previous
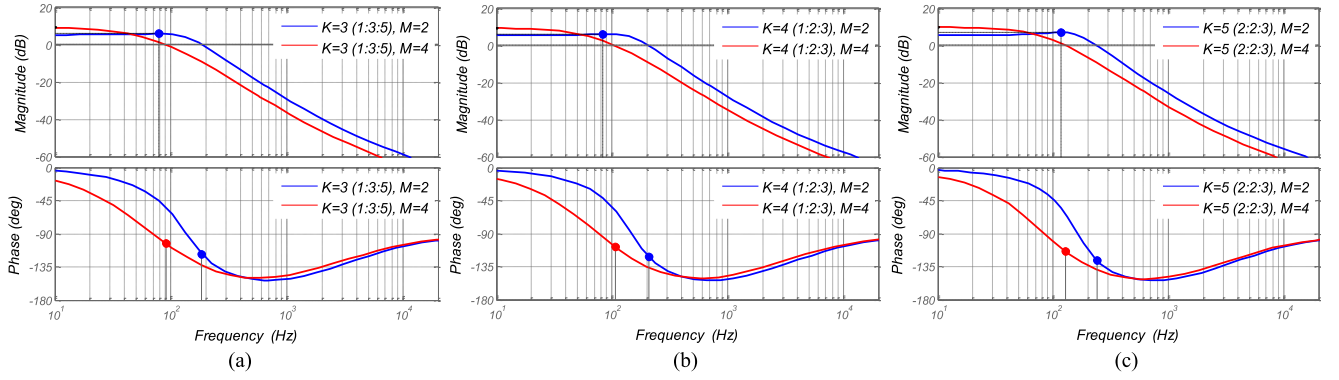
Fig. 20.   Bode plot for input to capacitor voltage transfer function of PWM Y-source converter with various winding factors and voltage gains.
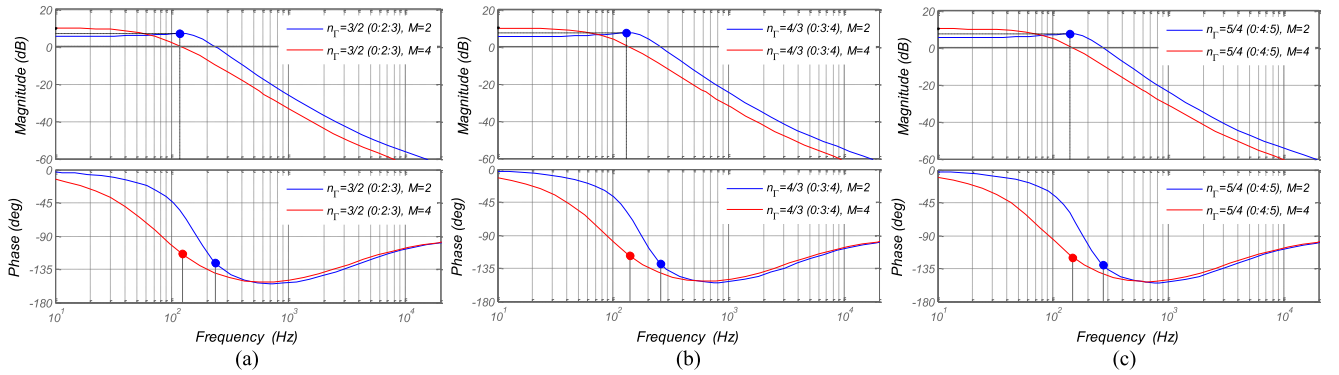

Fig. 21.   Bode plot for input to capacitor voltage transfer function of PWM Γ-source converter various with turns ratios and voltage gains.
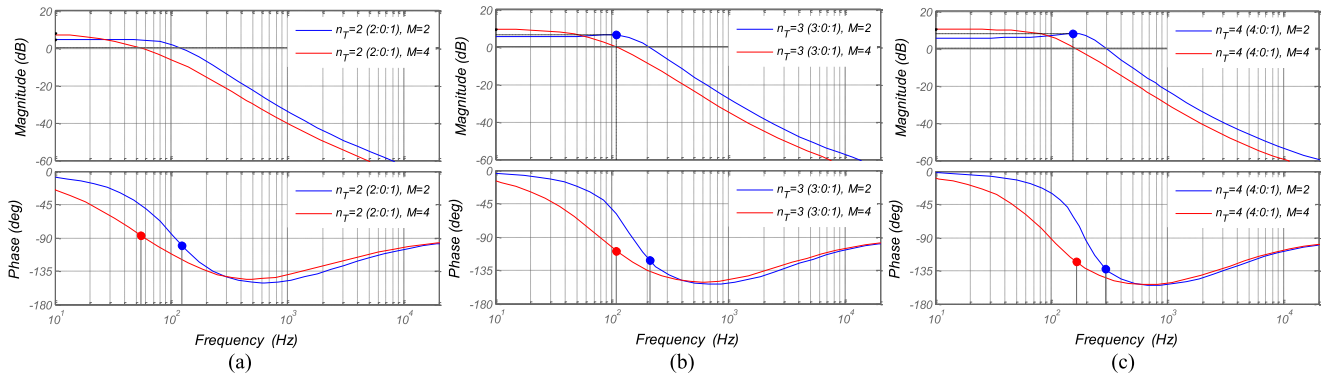

Fig. 22.   Bode plot for input to capacitor voltage transfer function of PWM T-source converter with various turns ratios and voltage gains.

subsections. A summary of parameter variations on the dynamic and stability of MCIS converters is summarized in Table IV. Regarding to the poles and zeros placement, because the real pole and zero are near each other; hence, mostly they do not have a significant impact on the system dynamics. While the conjugate pole pairs mostly affect the dynamic of the system and the RHP zero placement demonstrate a well insight of the system stability.

E. Stability Margin Comparison

   In this section, effect of change in duty cycle on stability margin for various winding factors and turns ratios of the three

PWM MCIS converters has been investigated. As it is known, the stability of a NMP system is strictly related to its controller design and this paper is not dedicated to loop compensation of the mentioned converters. Hence, in order to compare the stability margin of MCIS converters, the G_{Vcv} transfer function that inherits a stable open loop is considered for the stability assessment of in this section. Bode plot for the G_{Vcv} transfer function of the PWM Y-source converter with different winding factors for $M = 2$ and $M = 4$ is depicted in Fig. 20. For each winding factor, the winding turns are selected from Table I. As mentioned before, with various windings combination $(N_1 : N_2 : N_3)$ for a specific K, the corresponding

TABLE V
COMPARISON BETWEEN FREQUENCY RESPONSE PWM MCIS CONVERTERS

	PM of PWM Y-source		PM of PWM Γ-source		PM of PWM T-source	
	$M = 2$	$M = 4$	$M = 2$	$M = 4$	$M = 2$	$M = 4$
$K = 3$ $n_\Gamma = 3/2$ $n_T = 2$	62.7	77.1	53.3	66.1	79.5	93.3
$K = 4$ $n_\Gamma = 4/3$ $n_T = 3$	58.7	72.1	50.7	62.2	58	71.3
$K = 5$ $n_\Gamma = 5/4$ $n_T = 4$	53.7	65.8	49.3	60.1	46.9	56.7

TABLE VI
PARAMETERS OF MCIS NETWORKS USED WITH PWM DC–DC CONVERTER
FOR EXPERIMENTS

Parameter/Description		Value
Input voltage (V_{IN})		15 V
Load	Resistance (R_o)	40 Ω
	Inductance (L_o)	2.3 mH
Switching frequency (f_s)		25 kHz
Shoot-through duty cycle (D)		8%
Capacitor C	Capacitance	470 μF
	ESR	85 mΩ
Turns Ratio of coupled inductors	Y-source network ($N_1 : N_2 : N_3$)	15:30:45 on C055710A2 core
	Γ-source network ($N_2 : N_3$)	30:40 on C055710A2 core
	T-source network ($N_1 : N_3$)	60:20 on C055710A2 core
Winding inductance of coupled inductors	Y-source network ($L_1 : L_2 : L_3$)	$(86 : 334 : 710)\ \mu H$
	Γ-source network ($L_2 : L_3$)	$(347 : 633)\ \mu H$
	T-source network ($L_1 : L_3$)	$(1392 : 158)\ \mu H$
Winding resistance of coupled inductors	Y-source network ($R_1 : R_2 : R_3$)	$(64 : 230 : 490)\ m\Omega$
	Γ-source network ($R_2 : R_3$)	$(244 : 457)\ m\Omega$
	T-source network ($R_1 : R_3$)	$(836 : 88)\ m\Omega$
Switch S		C2M0080120D
Diode D		C3D25170H

Fig. 23. Schematic of the experimental setup to measure G_{Vcv} and G_{Vcd} of various MCIS network topologies.

Fig. 24. Picture of the experimental setup for frequency measurements of PWM MCIS converters.

frequency responses of the PWM Y-source converter may have some slight differences.

Bode plots for the G_{Vcv} transfer function of the PWM Γ-source and PWM T-source converters are illustrated in Figs. 21 and 22, respectively. It is worth to mention that the bode plots of in Figs. 21 and 22 are drawn using the G_{Vcv} transfer function of the PWM Y-source converter and letting the first (N_1) and the second (N_2) windings equal to zero, respectively.

The measured PM of the mentioned PWM MCIS converters is summarized in Table V. Notably, the numerical values are not of interest on their own, the relations and trends of values are more interesting in this assessment. Regarding stability margin for PWM MCIS converters, by increase in the winding factor for both high- and low-gain conditions, the PM decreases. In high-gain condition, the stability margin for G_{Vcv} is higher than of in
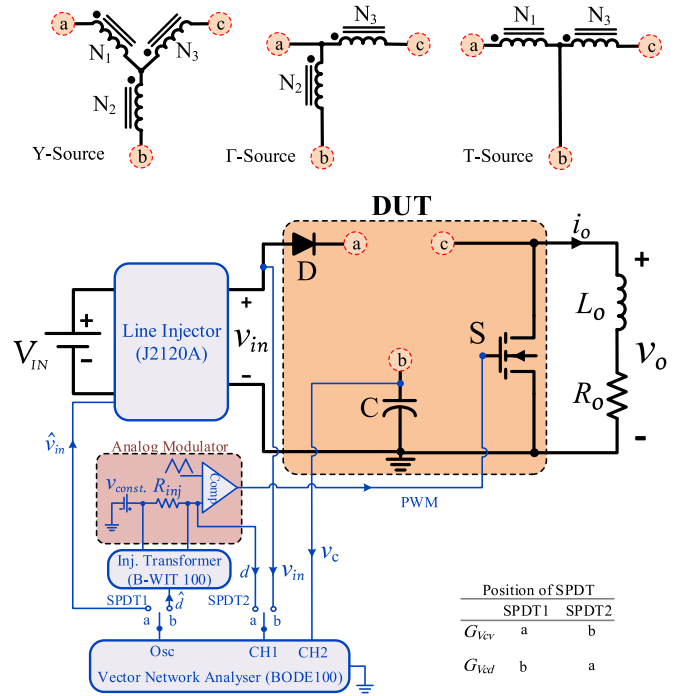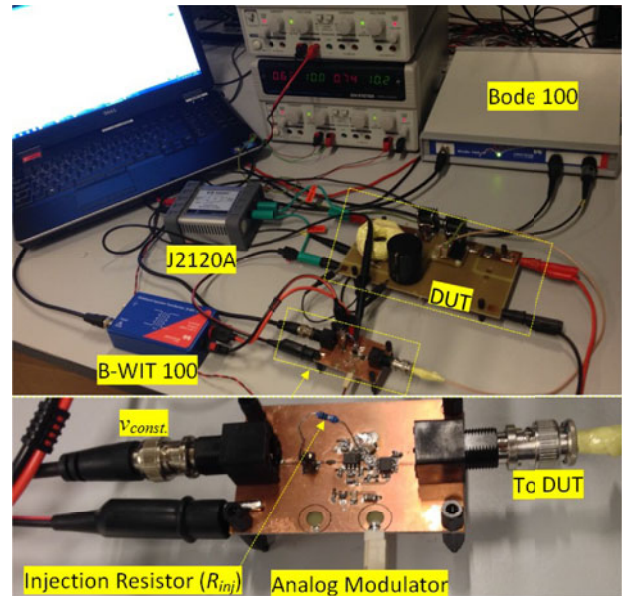
low-gain condition. It is worth to mention this is different from pole-zero analysis of G_{Vcd} in previous sections. Obviously, the PM for G_{Vcv} of the PWM Γ-source converter is lower than of in two other PWM converters. Furthermore, for both voltage gain conditions, the largest change in PM are related to the PWM T-source and the slightest change in PM is related to the PWM Γ-source. This is mainly due to the assumption of an identical total inductance (L) and parasitic resistance (ESR$_T$) for all converters, which put a higher magnetizing inductance and

Fig. 25. Experimentally obtained frequency responses and corresponding simulated results for (a) input to capacitor voltage and (b) control to capacitor voltage transfer functions of the PWM Y-source converter.
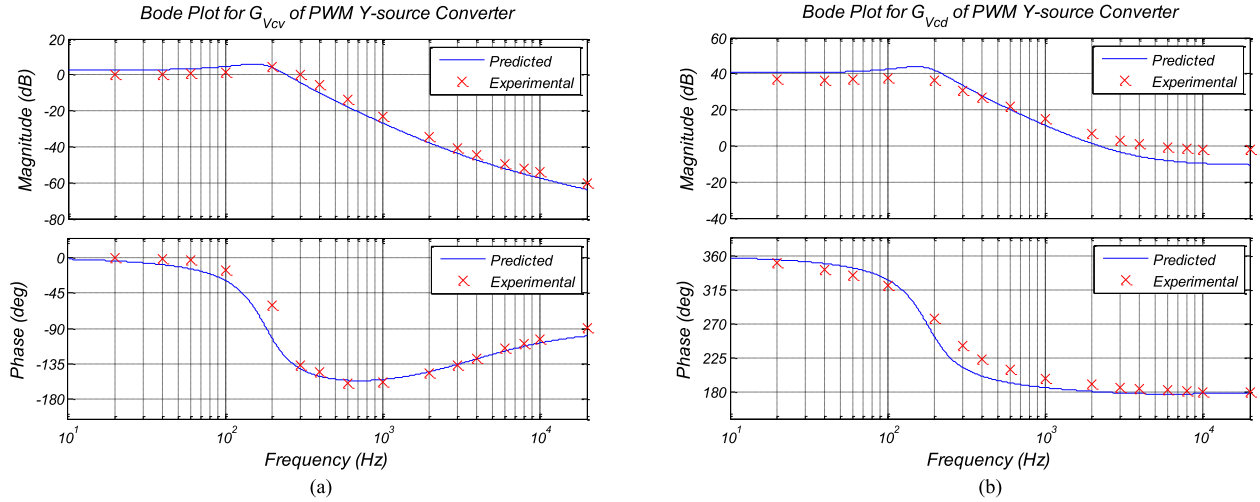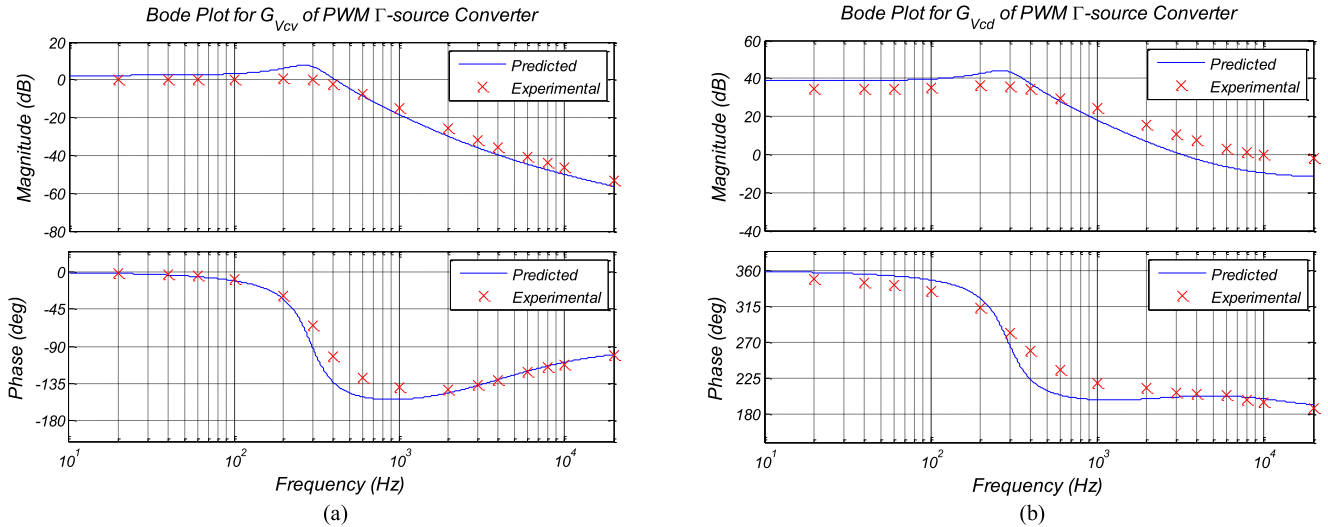

Fig. 26. Experimentally obtained frequency responses and corresponding simulated results for (a) input to capacitor voltage and (b) control to capacitor voltage transfer functions of the PWM Γ-source converter.

parasitic resistance on the third winding of the PWM Γ-source converter than on two other converters.

Regarding the peak magnitude ($M_{\rm PK}$) of the PWM MCIS converters, it can be seen that by increase in K and n_T (decrease in n_Γ), the $M_{\rm PK}$ increased slightly, which lead to low damping effect in the dynamic response of those converters. However, due to distributed windings ratio and the assumption of identical total inductance, the change in $M_{\rm PK}$ of the PWM Γ-source is barely noticeable. From Fig. 20 to Fig. 22, it can be seen that the corner frequency ($f_{\rm c}$) of those converters in low-voltage gain situations is higher than in high-voltage gain situations and in both voltage gains, the $f_{\rm c}$ increases by increase in turns ratios. The largest change in $f_{\rm c}$ is related to the PWM T-source and the slightest change in $f_{\rm c}$ is related to the PWM Γ-source. As expected, these general analytical assessments are in agreement with the previous discussions.

VI. EXPERIMENTAL RESULTS

In order to verify the effectiveness of derived transfer functions, some measurements have been done for the mentioned PWM MCIS converter. A configurable prototype of the PWM MCIS converters has been designed and built in the laboratory. In consequent, various coupled inductors was wound on separate molypermalloy powder toroid cores for Y-source, Γ-source, and T-source networks. Detailed parameters used for experiment are shown in Table VI.

Schematic drawing of the experimental setup to measure the frequency response is shown in Fig. 23. Bode 100 vector network analyzer was used to measure the transfer function gain phase of PWM MCIS dc–dc converters (bode plots). The frequency measurement of the derived transfer functions are comprised of two different phase, with perturbation in input voltage ($\hat{v}_{\rm in}$) and with perturbation in duty cycle ($\hat{d}$). In order to
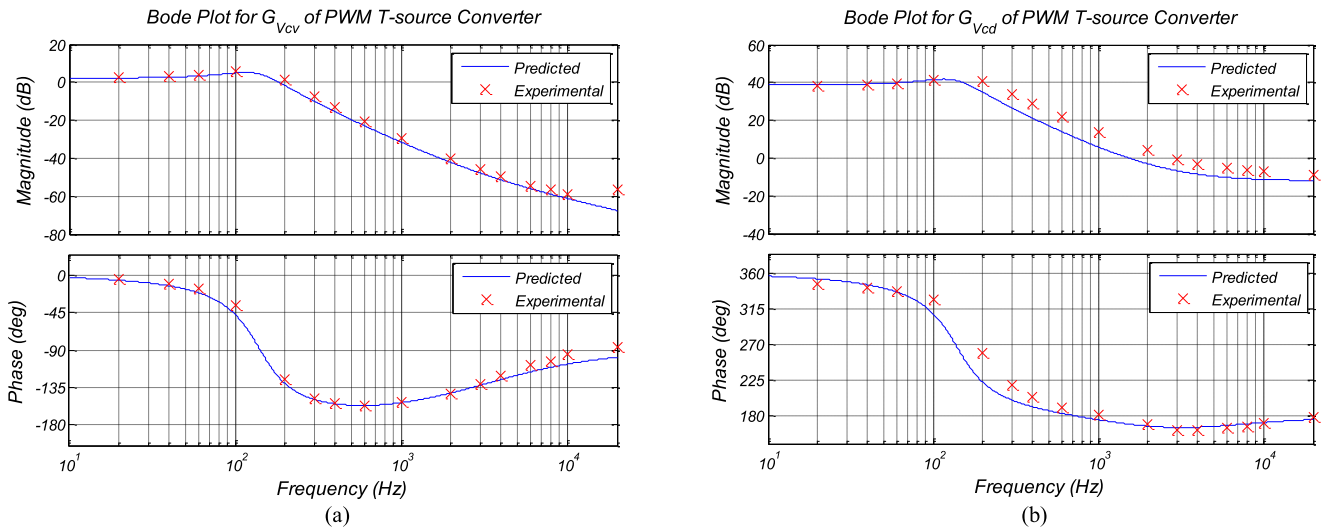
Fig. 27. Experimentally obtained frequency responses and corresponding simulated results for (a) input to capacitor voltage and (b) control to capacitor voltage transfer functions of the PWM T-source converter.
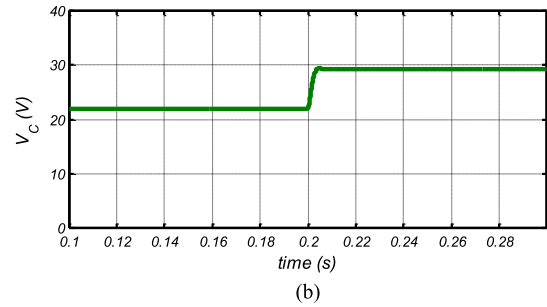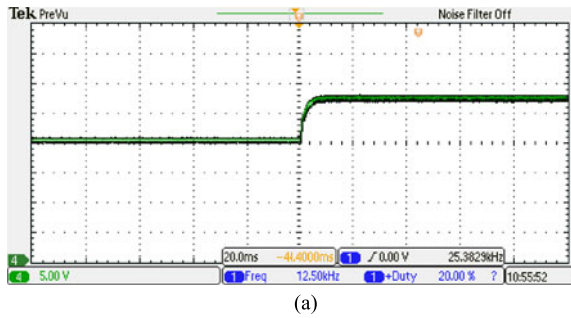

Fig. 28. Dynamic response of the PWM Y-source dc–dc converter to a step change in input voltage from 15 to 20 V: (a) Experimentally obtained and (b) theoretically predicted.
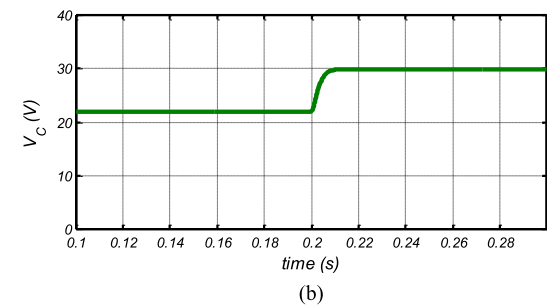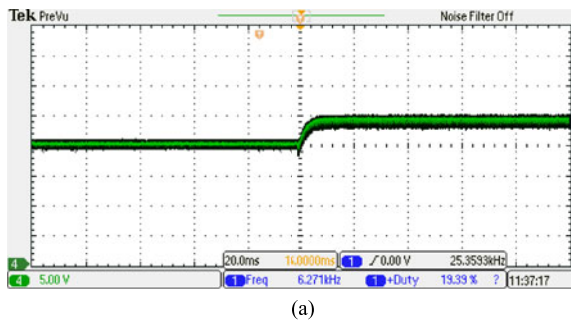

Fig. 29. Dynamic response of the PWM Y-source dc–dc converter to a step change in duty cycle from 0.1 to 0.15: (a) Experimentally obtained and (b) theoretically predicted.

inject the ac small signal to the input voltage a J2120A transformer was employed as a line injector. An analogue modulator with Texas Instrument TLV3502 comparator was built to generate PWM for the switch. The ac small signal generated by Bode 100 for duty cycle is injected through a B-WIT 100 injection transformer and an injection resistor (R_{inj}). Moreover, the single pole double throw (SPDT) switches (SPDT1 and SPDT2) define the appropriate connections of the measuring instrument to the device under test to measure the input to capacitor voltage

(G_{Vcv}) and control to capacitor voltage (G_{Vcd}) transfer functions. A picture of the measurement setup implemented in the laboratory is shown in Fig. 24.

The measured frequency responses for the PWM Y-source converter are shown in Fig. 25. In which the experimental results are shown with cross marks along with the theoretically predicted results from the derived transfer functions including the ESRs of inductor and capacitor. As clearly can be seen both experimental and simulation results are in good

agreement. This convincing behavior for the system is owing to the fact that the parasitic resistances are included in those derived transfer functions. Figs. 26 and 27 illustrate the frequency response for the PWM Γ-source and PWM T-source converters, respectively. Same as the PWM Y-source converter, the theoretically predicted results for PWM Γ-source and PWM T-source converters are in good agreement with the experimental results obtained from Bode 100. This close correspondence verifies the derived transfer functions and theoretical analysis made in earlier sections.

In order to see dynamic behavior of the PWM MCIS dc–dc converters, dynamic response of the PWM Y-source converter is considered as an example that corresponds to the other two winding MCISs. Fig. 28 illustrates the experimentally along with the theoretically obtained dynamic response for the PWM Y-source dc–dc converter to a step change in input voltage from 15 to 20 V. Fig. 29 illustrates the experimentally along with the theoretically obtained dynamic response for the PWM Y-source converter to a step change in duty cycle from 0.1 to 0.15. The circuit parameters of computer simulation are identical to the parameters of experimental setup. Moreover, to be compatible with the experimental setup, 1.1-Ω measured resistance from the input of the coupled inductors, which corresponds to loosely connected wires and connections of in the dynamic response, is also considered in the averaged model. In Fig. 29, a voltage dip can be seen just before the capacitor voltage starts to raise, which can be attributed to the NMP effect of the control to capacitor voltage transfer function. It should be mentioned that because of neglecting switching power loss in the averaged circuit model, there is a small difference between the experimental and simulation results, which due to the increased loss in high duty cycle this difference is more considerable in Fig. 29. The dynamic response of the rest of the PWM MCIS converters follows similar behavior as of Y-source network with the step change in input voltage and duty cycle, so due to brevity only response of Y-source network is presented.

VII. Conclusion

This paper provides a generalized structure for small-signal modeling of MCIS converters. The derivation of relevant transfer functions has been done in their general form for the PWM Y-source converter and the transformation to a PWM Γ-source and a PWM T-source converter has been demonstrated. Furthermore, in this paper, the large-signal averaged model, dc and ac small-signal model of PWM MCIS converters have been demonstrated. All derived transfer functions have been validated via frequency and dynamic responses through simulation results. In the second part of this paper, a comprehensive analysis of the impact of different parameter variations on the dynamic and stability of those converters have been presented. In addition, some conceptual and analytical comparisons between the studied PWM MCIS converters are demonstrated. Finally, the validity of the derived transfer functions has been verified through experimental results from Bode 100 vector network analyzer for all mentioned PWM MCIS converters.

References

[1] Y. P. Siwakoti, F. Z. Peng, F. Blaabjerg, P. C. Loh, and E. Graham Town, "Impedance source network for electric power conversion—Part I: A topological review," *IEEE Trans. Power Electron.*, vol. 30, no. 2, pp. 699–716, Feb. 2015.

[2] P. C. Loh, D. Li, and F. Blaabjerg, "Γ-Z-source inverters," *IEEE Trans. Power Electron.*, vol. 28, no. 11, pp. 4880–4884, Nov. 2013.

[3] R. Strzelecki, M. Adamowicz, N. Strzelecka, and W. Bury, "New type T-source inverter," in *Proc. Compat. Power Electron.*, 2009, pp. 191–195.

[4] Y. P. Siwakoti, P. C. Loh, F. Blaabjerg, and G. E. Town, "Y-source impedance network," *IEEE Trans. Power Electron.*, vol. 29, no. 7, pp. 3250–3254, Jul. 2014.

[5] P. C. Loh and F. Blaabjerg, "Magnetically coupled impedance-source inverters," *IEEE Trans. Ind. Appl.*, vol. 49, no. 5, pp. 2177–2187, Sep./Oct. 2013.

[6] Y. Siwakoti, F. Blaabjerg, and P. C. Loh, "New magnetically coupled impedance (Z-) source networks," *IEEE Trans. Power Electron.*, Oct. 2016, to be published.

[7] R. Middlebrook and S. Ćuk, "A general unified approach to modelling switching-converter power stages," in *Proc. IEEE Power Electron. Spec. Conf.*, 1970, pp. 18–34.

[8] V. Vorperian, "Simplified analysis of PWM converters using model of PWM switch. Continuous conduction mode," *IEEE Trans. Aerosp. Electron. Syst.*, vol. 26, no. 3, pp. 490–496, Mar. 1990.

[9] K. Smedley and S. Ćuk, "Switching flow-graph nonlinear modeling technique," *IEEE Trans. Power Electron.*, vol. 9, no. 4, pp. 405–413, Apr. 1994.

[10] F. L. Luo and H. Ye, "Small signal analysis of energy factor and mathematical modeling for power DC–DC converters," *IEEE Trans. Power Electron.*, vol. 22, no. 1, pp. 69–79, Jan. 2007.

[11] R. W. Erickson and D. Maksimovic, *Fundamentals of Power Electronics*, 2nd ed. Norwell, MA, USA: Kluwer, 2001.

[12] M. K. Kazimierczuk, *Pulse-Width Modulated DC-DC Power Converters*, 1st ed. London, U.K.: Wiley, 2008.

[13] Y. P. Siwakoti, F. Z. Peng, F. Blaabjerg, P. C. Loh, G. E. Town, and S. Yang, "Impedance-source networks for electric power conversion part II: Review of control and modulation techniques," *IEEE Trans. Power Electron.*, vol. 30, no. 4, pp. 1887–1906, Apr. 2015.

[14] C. J. Gajanayake, D. M. Vilathgamuwa, and P. C. Loh, "Small-signal and signal-flow-graph modeling of switched Z-source impedance network," *IEEE Trans. Power Electron.*, vol. 3, no. 3, pp. 111–116, Sept. 2005.

[15] J. Liu, J. Hu, and L. Xu, "Dynamic modeling and analysis of Z-source converter—Derivation of AC small signal model and design-oriented analysis," *IEEE Trans. Power Electron.*, vol. 22, no. 5, pp. 1786–1796, Sept. 2007.

[16] Y. Li, S. Jiang, J. G. Cintron-Rivera, and F. Z. Peng, "Modeling and control of quasi-Z-source inverter for distributed generation applications," *IEEE Trans. Ind. Electron.*, vol. 60, no. 4, pp. 1532–1541, Apr. 2013.

[17] V. P. N. Galigekere and M. K. Kazimierczuk, "Small-signal modeling of open-loop PWM Z-source converter by circuit-averaging technique," *IEEE Trans. Power Electron.*, vol. 28, no. 3, pp. 1286–1296, Mar. 2013.

[18] M. M. Bajestan, M. A. Shamsinejad, and D. A. Khaburi, "Derivation of AC small signal model and analysis of trans-Z-source inverter," in *Proc. Iranian Conf. Electr. Eng.*, 2015, pp. 1624–1629.

[19] Z. Yuming, X. Dianguo, Z. Donglai, T. Wen, and H. Junping, "Modeling and control of the improved trans-Z-source inverter," in *Proc. IEEE Conf. Ind. Electron. Appl.*, 2014, pp. 650–654.

[20] L. Jingbo, H. Jiangang, and X. Longya, "A modified space vector PWM for Z-source inverter-modeling and design," in *Proc. Int. Conf. Electr. Mach. Syst.*, 2005, pp. 1242–1247.

[21] P. C. Loh, D. M. Vilathgamuwa, C. J. Gajanayake, L. Y. Rong, and T. C. Wern, "Transient modeling and analysis of pulse-width modulated Z-source inverter," *IEEE Trans. Power Electron.*, vol. 22, no. 2, pp. 498–507, Mar. 2007.

[22] X. Ding, Z. Qian; S. Yang, B. Cui, and F. Z. Peng, "A direct peak dc-link boost voltage control strategy in Z-source inverter," in *Proc. IEEE Appl. Power Electron. Conf.*, 2007, pp. 648–653.

[23] C. J. Gajanayake, D. M. Vilathgamuwa, and P. C. Loh, "Development of a comprehensive model and a multiloop controller for Z-source inverter dg systems," *IEEE Trans. Ind. Electron.*, vol. 54, no. 4, pp. 2352–2359, Aug. 2007.

[24] G. Sen and M. E. Elbuluk, "Voltage and current-programmed modes in control of the Z-source converter," *IEEE Trans. Ind. Appl.*, vol. 46, no. 2, pp. 680–686, Mar./Apr. 2010.

[25] O. Ellabban, J. Van Mierlo, and P. Lataire, "A DSP-based dual-loop peak DC-link voltage control strategy of the Z-source inverter," *IEEE Trans. Power Electron.*, vol. 27, no. 9, pp. 4088–4097, Sep. 2012.

[26] M. Forouzesh and A. Baghramian, "Galvanically isolated high gain Y-source DC-DC converters for dispersed power generation," *IET Power Electron.*, vol. 9, no. 6, pp. 1192-1203, 2016.

[27] K. M. Smedley, "Control art of switching converters," Ph.D. dissertation, Dept. Electr. Eng., California Inst. Technol., Pasadena, CA, USA, 1991.

[28] R. W. Erickson, "Optimal single resistor damping of input filters," in *Proc. IEEE Appl. Power Electron. Conf.*, 1999, pp. 1073–1079.

[29] S. Skogestad and I. Postlethwaite, *Multivariable Feedback Control: Analysis and Design*, 2nd ed. New York, NY, USA: Wiley, 2001.

[30] B. Bao, J. Yang, J. Xu, X. Zhang, and G. Zhou, "Effect of output capacitor ESR on dynamic performance of voltage-mode hysteretic controlled buck converter," *Electron. Lett.*, vol. 49, no. 20, pp. 1293–1294, Sep. 2013.

Mojtaba Forouzesh (S'14) received the B.S. degree in physics and the M.S. degree in electrical engineering (with highest honor) from the University of Guilan, Rasht, Iran, in 2011 and 2015, respectively.

He is currently working on several research studies in collaboration with Aalborg University, Aalborg, Denmark. His major research interests include magnetically coupled impedance source based converters/inverters, high step-up dc-dc converters, renewable energy technologies and applications, small signal modeling of power converters and digital implementation of modulation and control schemes.

Mr. Forouzesh is a member of the IEEE Power Electronics and Industrial Electronics societies, and a frequent reviewer for ECCE2016, INTELEC2016 and PEDG2016 conferences, and the *IET Power Electronics* and the Wiley *International Journal of Circuit Theory and Applications*.

Yam P. Siwakoti (S'10–M'14) received the B.Tech. degree in electrical engineering from the National Institute of Technology, Hamirpur, India, in 2005, the M.E. degree in electrical power engineering (magna-cum-laude) from the Norwegian University of Science and Technology, Trondheim, Norway, and Kathmandu University, Dhulikhel, Nepal, in 2010, and the Ph.D. degree from Macquarie University, Sydney, N.S.W., Australia, in 2014.

Since November 2014, he has been a Postdoctoral Researcher at the Department of Energy Technology, Aalborg University, Aalborg, Denmark. His research interests include modeling and design of high-power density converter; investigate new power converter topology with higher efficiency, reliability, and power density; application of new widebandgap semiconductor devices (GaN/SiC) for VHF power converter and wireless power transfer.

Dr. Siwakoti is an Associate Editor of the *IET Power Electronics* and a Guest Associate Editor of the IEEE TRANSACTIONS ON POWER ELECTRONICS Special Issues on the Impedance-Source Converter Topologies and Applications. He received an award by the IEEE TRANSACTIONS ON POWER ELECTRONICS as an Outstanding Reviewers of 2015.

Frede Blaabjerg (S'86–M'88–SM'97–F'03) from 1988 to 1992, he was a Ph.D. Student with Aalborg University, Aalborg, Denmark.

He was with ABB-Scandia, Randers, Denmark, from 1987 to 1988. He became an Assistant Professor in 1992, Associate Professor in 1996, and Full Professor of power electronics and drives in 1998. His current research interests include power electronics and its applications, such as in wind turbines, PV systems, reliability, harmonics, and adjustable speed drives.

Dr. Blaabjerg has received 17 IEEE Prize Paper Awards, the IEEE PELS Distinguished Service Award in 2009, the EPE-PEMC Council Award in 2010, the IEEE William E. Newell Power Electronics Award in 2014, and the Villum Kann Rasmussen Research Award in 2014. He was an Editor-in-Chief of the IEEE TRANSACTIONS ON POWER ELECTRONICS from 2006 to 2012. He is nominated in 2014 and 2015 by Thomson Reuters to be between the most 250 cited researchers in Engineering in the world.

Sara Hasanpour received the B.S. degree in electrical engineering from Azad Islamic University, Lahijan Branch, Iran, in 2002, and the M.S. degree from the Isfahan University of Technology, Isfahan, Iran, in 2005. She is currently working toward the Ph.D. degree at the Department of Electrical Engineering, University of Guilan, Rasht, Iran.

She is also a Lecturer at Azad Islamic University, Ramsar Branch, Ramsar, Iran. Her major research interests include control and modeling of dc–dc converters, electronic ballast, flexible ac transmission systems, sliding mode control, and digital signal processing.